

Testing multiflavored ultralight dark matter models with SPARC

Lauren Street¹*


*Fermi National Accelerator Laboratory, Batavia, Illinois 60510, USA
and Department of Physics, University of Cincinnati, Cincinnati, Ohio 45221 USA*

Nickolay Y. Gnedin²

*Fermi National Accelerator Laboratory, Batavia, Illinois 60510, USA;
Kavli Institute for Cosmological Physics, The University of Chicago, Chicago, Illinois 60637 USA
and Department of Astronomy and Astrophysics, The University of Chicago, Chicago, Illinois 60637 USA*

L. C. R. Wijewardhana

Department of Physics, University of Cincinnati, Cincinnati, Ohio 45221 USA

 (Received 15 April 2022; accepted 25 July 2022; published 5 August 2022)

We perform maximum likelihood estimates for single and double flavor ultralight dark matter (ULDM) models using the Spitzer Photometry and Accurate Rotation Curves database. These estimates are compared to maximum likelihood estimates for several commonly used cold dark matter (CDM) models. By comparing various CDM models we find, in agreement with previous studies, that the Burkert and Einasto models tend to perform better than other commonly used CDM models. We focus on comparisons between the Einasto and ULDM models and analyze cases for which the ULDM particle masses are fixed or free to vary. For each of these analyses, we perform fits assuming the soliton and halo density profiles are summed together or matched at a given radius. Letting the particle masses vary and assuming the summed models, we find a negligible preference for any particular range of particle masses within $10^{-25} \text{ eV} \leq m \leq 10^{-19} \text{ eV}$. For the matched models, we find that almost all galaxies prefer particle masses in the range $10^{-23} \text{ eV} \lesssim m \lesssim 10^{-20} \text{ eV}$. For both double flavor models we find that most galaxies prefer approximately equal particle masses. Fixing the particle masses, we find the best fit results for the particle mass $m = 10^{-20.5} \text{ eV}$, assuming the single flavor models, and $m_1 = 10^{-20.5} \text{ eV}$, $m_2 = 10^{-20.2} \text{ eV}$, assuming the double flavor, matched model.

DOI: [10.1103/PhysRevD.106.043007](https://doi.org/10.1103/PhysRevD.106.043007)

I. INTRODUCTION

A persistent problem in physics is the physical nature of dark matter (DM). A popular candidate is cold dark matter (CDM) which is thought to envelope galaxies far beyond the reaches of baryonic matter. On galactic scales, the presence of CDM is thought to be the cause of flat rotation curves at large radii. However, past CDM-only simulations resulted in galactic halo profiles (Navarro-Frenk-White (NFW) profiles [1–3]) that tended to be poor fits to the density profiles of low mass and low surface brightness galaxies; a problem which has commonly become known as the “cusp-core” problem. These galaxies tended to have more cored profiles, such as the Burkert [4] profile; which are constant near small radii and asymptote to the NFW profile for large radii. For reviews on the cusp core as well as other “small-scale” problems of CDM see references [5,6]. For a review on baryonic solutions to problems with CDM see [7].

It has been recently suggested that the Burkert profile is also a better fit for larger galaxies compared to the NFW profile [8]. Another recent study [9] has shown that the Einasto profile is a better fit to the galaxies in the Spitzer Photometry and Accurate Rotation Curves (SPARC) catalog [10] than the NFW profile. This suggests that the CDM only simulations that resulted in NFW profiles do not give an adequate picture of galactic DM halos. However, it has also been recently shown that simulated halos of CDM over a large range of masses can be fit well by the Einasto profile [11]. In this case, the cusp-core problem of the NFW profile can be resolved by noting that the cored Einasto profile can also be used to model simulated CDM only halos.

It is natural to think that baryonic matter and DM affect each other throughout the evolution of galaxies. There have been two main proposed baryonic solutions to the cusp-core problem which do well when confronted with data [6]. These two solutions both act to reduce the DM density in the inner regions of DM halos: one through supernova feedback flattening [12–15]; and the other through

*streetlg@mail.uc.edu

dynamical friction from baryonic clumps [16–18]. This reduction of the DM density helps to resolve not only the cusp-core problem, but other small-scale problems of CDM, including the “too big to fail” and the “missing satellites” problems for halo masses $M > 10^6 M_\odot$ for supernova feedback flattening and $M > 10^5 M_\odot$ for dynamical friction from baryonic clumps.

Recent hydrodynamical simulations suggest that the behavior and shape of the cores of galaxies depend on the ratio of stellar and DM masses (M_*/M_{halo}) [19–24]. If this is the case, DM only simulations cannot properly describe the cores of galaxies. A recent study of simulated CDM halos with baryonic and stellar feedback mechanisms [25] has shown that, in fact, CDM with baryonic effects results in halos without the many of the small-scale problems of CDM only halos. A phenomenological density profile that takes into account M_*/M_{halo} , dubbed “DC14” [20,21], has recently been shown to be a much better fit to galactic data than the NFW profile [24]. It has also been shown that the DC14, as well as other cored profiles, generally give better fits to the galaxies in the SPARC catalog than the NFW profile [26]. Two other mass-dependent profiles have also recently been proposed: the Dekel-Zhao profile [27] which was tested on the NIHAO simulations and the core-Einasto profile [28] which was tested on the FIRE simulations. Both of these profiles do well in fitting both cored and cuspy profiles and perform better than the DC14 model.

While the cusp-core problem is now generally considered to be resolved, there is another problem with the traditional CDM only halo model, i.e., the NFW model, known as the “diversity” problem [29]. This describes the trend for galaxies with similar maximum circular velocities to exhibit a wide range of inner circular velocity profiles; a trend which is poorly modeled by the NFW profile. However, it has been shown that both modified Newtonian dynamics (MOND) models [30,31] as well as self-interacting dark matter (SIDM) models can be well fit to the diverse ranges of inner profiles [32–34].

In [33], it was shown that SIDM can be fit well to many of the galaxies in the SPARC catalog while also reproducing the concentration mass relation (CMR) [35], the abundance matching relation (AMR) [36,37], the baryonic Tully-Fisher relation (BTFR) [38], stellar synthesis models [39], and the gravitational radial acceleration relation (RAR) [40]. It has also been recently suggested that hadronically interacting DM (HIDM) models tend to fit the SPARC catalog galaxies better than traditional SIDM models [9].

Another popular candidate for DM is the QCD axion which was originally theorized to potentially solve the strong CP problem [41–43]. Similar types of particles, termed axionlike particles (ALPs), arise in string compactification and clockwork theories [44,45], usually such that many different ALPs are theorized to be in existence.

Modeling QCD axions and ALPs as DM has gained an increase in interest, partly due to the failure to discover weakly interacting massive particles in various searches.

On galactic and cosmological scales, QCD axions and ALPs act similarly to CDM. ALPs, which are bosonic, can naturally form gravitationally bound structures, commonly called solitons, on astrophysical scales, a subject which has been studied in great detail in the recent past [46–71]. A subset of ALPs, termed ultralight DM (ULDM), with masses of $m \sim 10^{-22}$ eV have Compton wavelengths on the order of galactic cores [72–82]. Because of this, these types of particles were theorized to make up the cores of galaxies, in an attempt to solve the small-scale problems, at the time, of CDM [83–91]. However, as noted previously, the small-scale problems of CDM tend to disappear when taking into account the relationship of baryonic matter and CDM in galaxies.

While ULDM with masses $m \sim 10^{-22}$ eV can potentially form structures on the order of galactic cores, single flavor models that consider these masses have increasingly become constrained [92–102]. There have been numerous, recent analyses constraining the ULDM mass from galactic data. Simulations of collapsing ULDM halos suggest a relationship between the mass of the soliton that forms in a galaxy, and the properties of its host halo, termed the soliton-halo (SH) relation.

In [95], it was shown that the SH relation implies that the maximum circular velocity of a soliton should be of the same order as the maximum circular velocity of its host halo. From this implication, the authors showed that low-surface brightness galaxies in the SPARC catalog disfavor the SH relation for ULDM masses of $m \sim 10^{-21}$ – 10^{-22} eV. The authors of [96] extended this analysis by including external gravitational potentials in order to understand the effect of baryons on the formation and structure of the soliton and host halo. The results of [95] were further confirmed with the analysis of [96] and another study [102] that we will describe in more detail later.

However, the authors of another recent study which highlights the discrepancies in the SH relations resulting from various simulations found an empirically derived SH relation with a dispersion that includes all previously derived SH relations [103]. The authors claim that any previously derived constraints on the soliton and halo parameters must include an additional uncertainty due to the increasing dispersion in the SH relation with increasing halo mass.

Other previous analyses have shown that ULDM masses $m \gtrsim 10^{-22}$ eV tend to give good fits for particular ultrafaint dwarf (UFD) satellites [104] while masses $m \lesssim 10^{-22}$ eV tend to give good fits for particular dwarf spheroidal (dsphs) [78,91,105]. However, the masses that can potentially fit UFDs give poor fits for dsphs, while the masses that can potentially fit the dsphs result in UFD masses that are too large. From the upper constraint on the UFD galaxy

masses, a lower constraint of $m > 10^{-21}$ eV can be placed on the ULDM mass [97].

In [101], a model independent analysis of the SPARC galaxies was done in which both lower and upper constraints could be placed on the ULDM mass. It was shown that the most constraining galaxy excluded the mass range of $m = (0.14-3.11) \times 10^{-22}$ eV. Finally, the analysis of [95] was extended by doing a systematic scan over possible ULDM masses [102]. In this analysis, a conservative constraint was put on the ULDM mass from SPARC catalog galaxies by finding the maximum possible mass of the soliton. It was shown that structures composed of ULDM masses in the range 10^{-24} eV $\lesssim m \lesssim 10^{-20}$ eV that satisfied the SH relation were in tension with the rotation curve data of the SPARC galaxies.

This analysis was model independent in the sense that the authors made no assumptions about the nature of the host halo. Rather, they only used galaxies that had circular velocities which were overshoot by the soliton circular velocity in order to place constraints. The authors also did a model dependent statistical fit to derive similar constraints using a log-likelihood ratio. For this fit, they assumed the host halo of the soliton could be described by either the NFW or Burkert profile and added the halo to the soliton in two ways. The first was by simply adding the two together, assuming both the soliton and halo profiles contribute to the galactic DM density, and the second was by matching the inner soliton profile to the outer halo profile at some transition radius. In both cases, the statistical analysis further confirmed the model independent constraint for ULDM masses in the range 10^{-24} eV $\lesssim m \lesssim 10^{-20}$ eV.

It is clear, then, that ULDM masses of $m \lesssim 10^{-20}$ eV are well constrained from galactic data. However, if one models ULDM as being composed of multiple species, as is natural in string and clockwork theories, these constraints can potentially be evaded or decreased. It is interesting, then, to consider the types of structures that are formed from multiple species on galactic scales. There have already been several studies to this effect [100,106–108], and one can directly compare the resulting models to galactic data in order to test the validity of galactic DM as multiple species of ULDM.

From a recent analysis [100], two main species of ULDM (with masses of $m_1 \sim 10^{-22}$ eV and $m_2 \sim 10^{-20}$ eV) have been inferred from dsphs and UFDs, respectively. It was also shown that the inner profile of the Milky Way (MW) can be fit to a combination of solitons each composed of a different mass, with one of the solitons making up the DM components of the MW nuclear star cluster. The possibility of a third species was also suggested from the analysis of the 47 Tuc globular cluster. This study assumed that each DM galactic structure (except for the MW) was composed of only one species of ULDM, while allowing different galaxies to be composed of different species of ULDM. The MW, however,

was modeled as being composed of ULDM structures formed from two different species.

Besides multiple flavors, ULDM galactic structures can also be composed of multiple energy eigenstates of a single flavor of ALP [109–114]. In fact, it has been suggested that these multistate systems perform better than single-state systems when compared to data [74,109–111,115–117]. We acknowledge that models of ULDM galactic halos composed of multiple energy eigenstates can also potentially fit galactic data, and we leave an analysis of these structures for future work. In another recent study [118], simulations of vector ULDM were shown to form structures similar to the core-halo structure of scalar ULDM. However, the structures formed exhibited a different SH relation and central density, resulting in the possibility of observational differences between vector and scalar ULDM.

It is evident, then, that there are multiple theories of galactic DM, including the following: CDM modeled with cored profiles, SIDM, and HIDM, each of which can potentially either describe many different types of galaxies or galactic empirical relations, or both. In this paper, we do not dispute the predictive power of any of these theories. Rather, we discuss theories of ULDM as galactic DM, since they are interesting alternatives to CDM, SIDM, HIDM, and MOND. ULDM galactic structures are theorized to have specific signatures and can potentially be searched for using pulsar timing arrays, with multiple flavored models of ULDM having more specific signatures than single flavored models of ULDM [119–122].

We compare ULDM models for both single and multiple flavored cases to commonly used CDM models of galactic DM halos using galactic rotation curves from the SPARC catalog.¹ We find the maximum likelihood parameters by minimization of the chi-square statistic and compare models to each other using the Bayesian information criterion (BIC) statistic, which penalizes models with more parameters. We also check which models, if any, are in tension with many empirically derived relations, including the CMR, the AMR, the BTFR, stellar synthesis models, and the gravitational RAR. We also check the SH relation for the ULDM models analyzed.

In Sec. II, we describe the galactic DM halo models that will be tested. In Sec. III, we describe the fitting procedure and we compare our analysis to previous studies in Sec. IV. We discuss our results and possible future implementations in Sec. V and conclude in Sec. VI. All results obtained in this paper can be found in the publicly available code [123]. Throughout the text, we use the notation $m_{22} = 10^{-22}$ eV.

¹We focus on ULDM models without self-interactions between the particles. For a common class of ULDM self-interaction potentials, it was shown that self-interactions could be neglected for all galactic halos in the SPARC catalog that were analyzed in [95]. We leave an analysis concerning different ULDM self-interaction potentials for future work.

II. DARK MATTER HALO MODELS

Here, we discuss the galactic DM halo models that will be tested against galactic data. We focus on four different models for CDM halos and the goodness of fit of each model is compared to each other as well as the ULDM models to be discussed later.

A. CDM

The halo model that resulted from CDM only simulations is the NFW model [1–3] which has a density profile given by

$$\rho_{\text{NFW}}(r) = \frac{\rho_s}{(r/r_s)[1 + (r/r_s)]^2}, \quad (2.1)$$

where ρ_s and r_s are some density and radius scale factors, respectively. A more phenomenologically motivated model is the Burkert model [4], which has a density profile given by

$$\rho_{\text{B}}(r) = \frac{\rho_s}{[1 + (r/r_s)][1 + (r/r_s)^2]}. \quad (2.2)$$

Another phenomenologically motivated model is the Einasto model [11,124,125] with a density profile given by

$$\rho_{\text{E}}(r) = \rho_s \exp \left\{ -\frac{2}{\alpha} \left[\left(\frac{r}{r_s} \right)^\alpha - 1 \right] \right\}, \quad (2.3)$$

where α is taken to be a free parameter. Finally, a model that takes into account the ratio of stellar to DM mass (M_*/M_{halo}) is the DC14 model [20,21] which has a density profile given by

$$\rho_{\text{DC14}}(r) = \frac{\rho_s}{(r/r_s)^\gamma [1 + (r/r_s)^\alpha]^{(\beta-\gamma)/\alpha}}, \quad (2.4)$$

where

$$\begin{aligned} \alpha &= 2.94 - \log_{10}[(10^{X+2.33})^{-1.08} + (10^{X+2.33})^{2.29}], \\ \beta &= 4.23 + 1.34X + 0.26X^2, \\ \gamma &= -0.06 - \log_{10}[(10^{X+2.56})^{-0.68} + (10^{X+2.56})], \\ X &= \log_{10} \left(\frac{M_*}{M_{\text{halo}}} \right). \end{aligned} \quad (2.5)$$

This above equation is only valid in the range $-4.1 < X < -1.3$. We constrain one of the fit parameters in order to ensure that $X < -1.3$. We note that there are two other mass-dependent profiles that perform better than the DC14 profile, namely the Dekel-Zhao profile [27] and the core-Einasto profile [28]. While there are various CDM profiles that can be compared, it is not practical to consider all of them in a single paper. Our choice of profiles to explore corresponds to those most commonly used as a

comparison profile in the literature on ULDM. However, it would be interesting to compare the ULDM models to the Dekel-Zhao and core-Einasto profile which we leave for future work.

For all CDM halos, we define the concentration, c_{200} , and virial velocity, V_{200} , as

$$c_{200} \equiv \frac{R_{200}}{r_s}, \quad V_{200} \equiv \sqrt{\frac{M_{200}}{M_P^2 R_{200}}}, \quad (2.6)$$

where $M_P \approx 1.22 \times 10^{19}$ GeV is the Planck mass, R_{200} is the radius at which the average density is equal to 200 times the critical density of the Universe ρ_c , and M_{200} is mass contained within R_{200} and is commonly called the virial mass. For each of the density profiles,

$$\begin{aligned} \rho_s &= \frac{M_{200}}{4\pi r_s^3 [\ln(1 + c_{200}) - \frac{c_{200}}{1+c_{200}}]}, \\ r_s &= \sqrt{\frac{3}{2\pi\rho_c} \frac{M_P V_{200}}{20c_{200}}}, \\ M_{200} &= \sqrt{\frac{3}{2\pi\rho_c} \frac{M_P^3 V_{200}^3}{20}}, \end{aligned} \quad (2.7)$$

where ρ_c is the critical density of the Universe. As in [24], we take the Hubble constant to be $H_0 = 73$ km/s/Mpc. For all profiles, we also take the total stellar mass to be

$$M_* \approx (\Upsilon_d + \Upsilon_b)L, \quad (2.8)$$

where Υ_d and Υ_b are the stellar mass-to-light ratios of the disk and bulge, respectively, and L is the total luminosity.

B. ULDM

Now, we discuss the ULDM models that will be fit to data and compared to each other as well as the CDM models. ULDM structures that resulted in simulations consisted of an inner ULDM soliton core and outer ULDM halo which could be approximated by the NFW profile [78,100]. Both the soliton and halo are composed of the same species of ULDM, while the soliton is in the form of a Bose-Einstein condensate, and the halo is in the form of virialized ULDM.

We focus on two cases: ULDM composed of a single species and ULDM composed of two species. For each of these, we take two possible models of the total galactic DM density profile: a sum of the soliton and halo density profiles; and the soliton density profile matched to the halo density profile at a particular radius. The second case is more physical, as this is the behavior that is expected from ULDM simulations [78,95,100,102]. However, the first case may be a valid description if one assumes that the

ULDM species only make up some portion of the total DM energy density [102].

While ULDM simulations clearly show structures that are well fit by a ULDM core matched to an NFW profile at some matching radius, we note that there have been no simulations analyzing the collapse of ULDM halos composed of multiple species. In this case, it is not clear whether the double flavor ULDM structures can be modeled as two solitons each matched to a halo. However, we choose to extrapolate the results of the single flavor ULDM simulations to double flavor models. The results of this study can then be compared to any future simulation analyses for double flavor models. It is also possible that each flavor of ULDM forms a BEC such that each BEC profile can be added together to form the core of the DM halo, which is then either summed or matched to the Einasto profile in the outer regions of the halo. This situation would presumably give different results from the case in which each soliton is matched or summed to a separate halo. It would also result in fewer fitting parameters, and we leave an analysis of this sort for future work.

For each analysis, we take the ULDM halo to follow the Einasto profile given by Eq. (2.3). Both the Einasto and Burkert profiles give overall better fits than the DC14 and NFW profiles, for the galaxies analyzed. We choose to use the Einasto profile instead of the Burkert profile due to its ability to fit simulated halos of CDM [11]. Finally, for each of these cases, we take the ULDM mass to be either a free parameter in the fitting procedure or fixed by scanning over particular values.

We analyze the profile of solitons composed of a single species and multiple species of ULDM. Solitons composed of a single species have the density profile as given in [78,95,100,102]

$$\rho_{\text{sol}}(r) \approx \frac{\rho_c}{(1 + 0.091(r/r_c)^2)^8}, \quad (2.9)$$

where

$$\rho_c \approx 7 \times 10^9 \left(\frac{M_{\text{sol}}}{10^9 M_{\odot}} \right)^4 \left(\frac{m}{m_{22}} \right)^6 \frac{M_{\odot}}{\text{kpc}^3}, \quad (2.10)$$

and

$$r_c \approx 0.228 \left(\frac{M_{\text{sol}}}{10^9 M_{\odot}} \right)^{-1} \left(\frac{m}{m_{22}} \right)^{-2} \text{kpc}, \quad (2.11)$$

with m the mass of the ULDM, M_{sol} the total mass of the soliton, and $m_{22} = 10^{-22}$ eV. Solitons composed of multiple species of ULDM have density profiles that can be approximated as a sum of the density profiles of single species structures [100]. In this analysis, we focus on two flavor models which result in a density profile given by

$$\rho_{\text{sol}}(r) \approx \sum_{i=1}^2 \rho_{\text{sol},i}(r), \quad (2.12)$$

where each of the $\rho_{\text{sol},i}$ is given by Eq. (2.9) and each species can have a different mass m_i .

Equation (2.9) is valid up to $r \sim 3r_c$ [78]. For the case in which we take the soliton profile to be matched to the halo profile, we take the transition radius to be $r_t = 3r_c$. For the single flavored model, the total galactic DM density profile is given by

$$\rho_{\text{Single}}^{\text{Matched}}(r) = \begin{cases} \rho_{\text{sol}}(r) & \text{if } r \leq 3r_c \\ \rho_{\text{halo}}(r) & \text{if } r \geq 3r_c \end{cases}, \quad (2.13)$$

where ρ_{sol} is given by Eq. (2.9) and we take ρ_{halo} to be given by the Einasto profile [Eq. (2.3)]. For the double flavored model, the total galactic DM density profile is given by

$$\rho_{\text{Double}}^{\text{Matched}}(r) = \begin{cases} \rho_{\text{sol},1}(r) + \rho_{\text{sol},2}(r) & \text{if } r \leq 3r_{c,1} \\ \rho_{\text{halo},1}(r) + \rho_{\text{sol},2}(r) & \text{if } 3r_{c,1} \leq r \leq 3r_{c,2} \\ \rho_{\text{halo},1}(r) + \rho_{\text{halo},2}(r) & \text{if } r \geq 3r_{c,2} \end{cases} \quad (2.14)$$

The relation

$$\rho_{\text{sol},i}(3r_{c,i}) = \rho_{\text{halo},i}(3r_{c,i}), \quad (2.15)$$

allows one free parameter to be fixed for the single flavor model and two for the double flavor model. For the single flavor model, we choose the Einasto halo profile variable α to be fixed, while for the double flavor model we choose each of the Einasto halo profile variables α_1 and α_2 to be fixed. We choose to solve for α from Eq. (2.15) since it can be solved analytically and we can use the same halo profile variables when assuming just CDM models (i.e., c_{200} and V_{200}).

For the case in which the soliton and halo profiles are summed together, we take the soliton profile to be valid for all r , as for $r > 3r_c$, the eighth power in the denominator causes the density profile to fall off rapidly. For the single flavored model, the total galactic DM density profile is given by

$$\rho_{\text{Single}}^{\text{Summed}}(r) = \rho_{\text{sol}}(r) + \rho_{\text{halo}}(r). \quad (2.16)$$

For the double flavored model, the total galactic DM density profile is given by

$$\rho_{\text{Double}}^{\text{Summed}}(r) = \sum_{i=1}^2 [\rho_{\text{sol},i}(r) + \rho_{\text{halo},i}(r)]. \quad (2.17)$$

It has been shown from simulations of collapsing halos consisting of a single species of ULDM that the core mass and halo mass follow a scaling relation given by [79,95]

$$M_{\text{sol}} \approx 1.4 \times 10^9 \left(\frac{m}{m_{22}}\right)^{-1} \left(\frac{M_{\text{halo}}}{10^{12} M_{\odot}}\right)^{1/3} M_{\odot}, \quad (2.18)$$

for halo masses, M_{halo} , greater than some minimal mass given by [95]

$$M_{\text{halo,min}} \sim 5.2 \times 10^7 \left(\frac{m}{m_{22}}\right)^{-3/2} M_{\odot}. \quad (2.19)$$

We do not impose this relation, rather we check that the constraint is satisfied after performing fits. As discussed above, it is unclear whether ULDM halos composed of multiple species will collapse to have the same structure as those composed of single flavor models. In this case, the SH relation may not even hold for double flavor models.

Finally, in a recent study [103], an SH relation that includes all previously derived SH relations was found and

$$V_{\text{bar}}(r) \equiv \sqrt{|V_{\text{gas}}(r)|V_{\text{gas}}(r) + \tilde{\Upsilon}_d|V_{\text{disk}}(r)|V_{\text{disk}}(r) + \tilde{\Upsilon}_b|V_{\text{bulge}}(r)|V_{\text{bulge}}(r)}, \quad (3.1)$$

where $\Upsilon_d = \tilde{\Upsilon}_d \Upsilon_*$ and $\Upsilon_b = \tilde{\Upsilon}_b \Upsilon_*$ are the stellar mass-to-light ratios of the disk and bulge.

In [10], the effect of choosing different values for $\tilde{\Upsilon}$ are explored, where the chosen values for the disk and bulge components are $\Upsilon_b = 1.4\Upsilon_d$. In our fitting procedure, we take both $\tilde{\Upsilon}_d$ and $\tilde{\Upsilon}_b$ as free parameters. From certain stellar synthesis models [39], the distribution of mass-to-light ratios of the disk and bulge are expected to peak at $\tilde{\Upsilon}_d = 0.5$ and $\tilde{\Upsilon}_b = 0.7$ for surface photometry at $3.6 \mu\text{m}$. In our fits, we take both mass-to-light ratios as free parameters, and check that the resulting distributions peak around the same values.

Assuming spherical symmetry of the DM halo, the DM contribution to the galactic rotation velocity at some distance r from the center of the galaxy is defined as

$$V_{\text{DM}}(r) \equiv \sqrt{\frac{4\pi \int_0^r dr' (r')^2 \rho_{\text{DM}}(r')}{M_{\tilde{p}}^2 r}}. \quad (3.2)$$

The total observed rotation velocity at a given radius can then be defined as

$$V_{\text{obs}}(r) \equiv \sqrt{V_{\text{DM}}(r)^2 + V_{\text{bar}}(r)^2}. \quad (3.3)$$

We use LMFIT: nonlinear least-square minimization and curve fitting for PYTHON [126] to find the maximum likelihood estimation (MLE) by minimization of the chi-square function and uncertainties: a PYTHON package for calculations with uncertainties [127] to handle the error calculations. The chi-square function minimized is given by

shown to have an increasing dispersion with increasing halo mass. While our results do not depend on the SH relation, we emphasize that if constraints were to be placed on any soliton and halo parameters by assuming the SH relation, an additional uncertainty from [103] would have to be taken into account.

III. ROTATION CURVES

The SPARC catalog [10] gives, at a given radius from the center of a galaxy, the total observed rotation velocity V_{obs} , the gas contribution to the rotation velocity V_{gas} , and the disk and bulge contributions to the rotation velocity, V_{disk} and V_{bulge} assuming a stellar mass-to-light ratio $\Upsilon_* = 1 M_{\odot}/L_{\odot}$. The contribution of baryonic matter to the total rotation velocity can then be defined as

$$\chi^2 = \sum_{i=1}^N \left(\frac{V_{\text{model}}(r_i, \tilde{p}) - V_i}{\sigma_i} \right)^2. \quad (3.4)$$

Here, V_i is the measured total circular velocity and σ_i is the error in the measured total circular velocity at the radius r_i , while $V_{\text{model}}(r_i, \tilde{p})$ is the modeled circular velocity for the parameter set \tilde{p} .

We test the significance of each model compared to each other model using the BIC statistic given by [26,128,129]

$$\text{BIC} \equiv -2 \ln(\mathcal{L}_{\text{MLE}}) + k \ln N, \quad (3.5)$$

where k is the number of parameters in the model and N is the number of data points. We take $\mathcal{L}_{\text{MLE}} \sim \exp(-\chi_{\text{MLE}}^2/2)$ where χ_{MLE}^2 is given by Eq. (3.4) with \tilde{p}_{MLE} the parameter set which gives the MLE. We find the difference in the BIC statistic between models, $\Delta\text{BIC} = \text{BIC}_{\text{model}_1} - \text{BIC}_{\text{model}_2}$, and use Jeffreys' scale [130] to test significance, where $2 < |\Delta\text{BIC}| \leq 6$ denotes mild evidence, $6 < |\Delta\text{BIC}| \leq 10$ denotes strong evidence, and $10 < |\Delta\text{BIC}|$ shows decisive evidence for model 1 (negative ΔBIC values) or model 2 (positive ΔBIC values). For $|\Delta\text{BIC}| \leq 2$, neither model is preferred.

We choose to compare the BIC statistic as well as the reduced chi-square statistic given by

$$\chi_v^2 = \chi^2 / (N - k), \quad (3.6)$$

where χ^2 is given by Eq. (3.4). The reduced chi-square tends to treat models similarly when the total number of data points is large compared to the number of model parameters. However, the BIC statistic tends to be more

TABLE I. Parameter ranges for each of the ULDM models tested: SS corresponds to the single flavor and DS to the double flavor, summed models; SM corresponds to the single flavor, and DM to the double flavor, matched models; models with (1) correspond to the analysis in which the particle masses are free to vary in the fitting procedure; models with (2) correspond to the analysis in which the particle masses are fixed. For the matched models, α_M corresponds to the value of alpha fixed from Eq. (2.15). For the models with (2), the values for m_1 and m_2 are fixed and the ranges quoted are scanned over during the fitting procedure.

Parameters	Models							
	SS(1)	SM(1)	DS(1)	DM(1)	SS(2)	SM(2)	DS(2)	DM(2)
$c_{200,1}$	$[1, 10^2]$	$[1, 10^2]$	$[1, 10^2]$	$[1, 10^2]$	$[1, 10^2]$	$[1, 10^2]$	$[1, 10^2]$	$[1, 10^2]$
$c_{200,2}$	$[1, 10^2]$	$[1, 10^2]$	$[1, 10^2]$	$[1, 10^2]$
$V_{200,1}$ [kms $^{-1}$]	$[1, 10^3]$	$[1, 10^3]$	$[1, 10^3]$	$[1, 10^3]$	$[1, 10^3]$	$[1, 10^3]$	$[1, 10^3]$	$[1, 10^3]$
$V_{200,2}$ [kms $^{-1}$]	$[1, 10^3]$	$[1, 10^3]$	$[1, 10^3]$	$[1, 10^3]$
\tilde{Y}_d	$[0.01, 5]$	$[0.01, 5]$	$[0.01, 5]$	$[0.01, 5]$	$[0.01, 5]$	$[0.01, 5]$	$[0.01, 5]$	$[0.01, 5]$
\tilde{Y}_b	$[0.01, 5]$	$[0.01, 5]$	$[0.01, 5]$	$[0.01, 5]$	$[0.01, 5]$	$[0.01, 5]$	$[0.01, 5]$	$[0.01, 5]$
α_1	$(-\infty, \infty)$	α_M	$(-\infty, \infty)$	α_M	$(-\infty, \infty)$	α_M	$(-\infty, \infty)$	α_M
α_2	$(-\infty, \infty)$	α_M	$(-\infty, \infty)$	α_M
m_1 [m_{22}]	$[10^{-3}, 10^3]$	$[10^{-3}, 10^3]$	$[10^{-3}, 10^3]$	$[10^{-3}, 10^3]$	$[10^{-3}, 10^3]$	$[1, 10^2]$	$10^{1.5}$	$10^{1.5}$
m_2 [m_{22}]	$[10^{-3}, 10^3]$	$[10^{-3}, 10^3]$	$[10^{-3}, 10^3]$	$[1, 10^2]$
$M_{\text{sol},1}$ [M_\odot]	$[10^{4.5}, 10^{12}]$	$[10^{4.5}, 10^{12}]$	$[10^{4.5}, 10^{12}]$	$[10^{4.5}, 10^{12}]$	$[10^{4.5}, 10^{12}]$	$[10^{4.5}, 10^{12}]$	$[10^{4.5}, 10^{12}]$	$[10^{4.5}, 10^{12}]$
$M_{\text{sol},2}$ [M_\odot]	$[10^{4.5}, 10^{12}]$	$[10^{4.5}, 10^{12}]$	$[10^{4.5}, 10^{12}]$	$[10^{4.5}, 10^{12}]$

conservative due to its stricter penalization of models with more parameters. Therefore, by comparing both the reduced chi-square and BIC for each model analyzed, we can potentially infer if the ULDM models with more parameters are significantly better fitting models than the CDM models with less parameters.

For each of the CDM and ULDM models we perform MLEs assuming uniform priors on all parameters. We also analyze other prior cases to test which galaxies or models are affected. We constrain any parameters that are constrained from physical arguments. For the DC14 model, we constrain the free parameter V_{200} such that $V_{200,\text{min}} \leq V_{200}$ where $V_{200,\text{min}}$ is found from the constraint that $\log_{10}(M_*/M_{\text{halo}}) < -1.3$. For the ULDM models in which the soliton and halo profiles are matched, we take α for the single flavor model and α_1 as well as α_2 for the double flavor model to be fixed from Eq. (2.15).

For the analysis case in which we assume uniform priors on all parameters, we perform the fits constraining the free parameters as $1 \leq c_{200} \leq 100$, $1 \leq V_{200}/[\text{km s}^{-1}] \leq 1000$, $0.01 \leq \tilde{Y}_d \leq 5$, and $0.01 \leq \tilde{Y}_b \leq 5$, all of which have been taken in previous studies. For the Einasto model, we take α to be unconstrained. We find that we get similar results when taking the constraints $5 \times 10^{-3} \leq \alpha \leq 5$. However, we leave the value of α unconstrained in order to allow more values for the ULDM models in which the soliton is matched to the halo.

For the ULDM models, we take $10^{4.5} \leq M_{\text{sol}}/M_\odot \leq 10^{12}$. When assuming the particle mass is free to vary in the fitting procedure, we take the particle masses within the range $10^{-3}m_{22} \leq m_i \leq 10^3m_{22}$. We take the same range for one of the particle masses for the case in which the particle masses are treated as fixed parameters.

We fix the other particle mass to $m = 10^{1.5}m_{22}$, as we find that approximately around this particle mass, we obtain the best results. After scanning this range, we find that only a small subset of masses produce reasonable fits for the ULDM models in which the soliton and halo are matched. Therefore, for these models, we perform a more detailed scan in the mass range $m_{22} \leq m \leq 10^2m_{22}$, while fixing the other mass to be $m = 10^{1.5}m_{22}$. We include a summary of all parameter ranges for the ULDM models tested in Table I.

For all analyses, we check that the CMR [11,35] is reproduced, that the resulting stellar and halo masses fit the AMR [36,37], that the baryonic mass and maximum circular velocity fit the BTFR [38], that the distribution of mass-to-light ratios is consistent with stellar synthesis models [39], and that the gravitational acceleration due to baryons and that due to DM fit the gravitational RAR of [40]. Each of these are described in more detail in Appendix A. For the ULDM models, we also check that the SH relation [Eq. (2.18)] is reproduced.

IV. COMPARISON WITH PREVIOUS STUDIES

We now discuss how our analysis compares to previous studies. First, we extend the results of [78,91,95–97, 101,102,104,105,131] by scanning over possible particle masses for double flavor ULDM models. While the authors of [102] discuss the possible constraints on multiple flavored models, they do not perform a systematic scan over particle masses for multiple flavored models. We therefore further their study by analyzing double flavor models and performing fits for all particle masses scanned.

We extend the results of these analyses by fitting 93 galaxies in the SPARC catalog to single and double flavor

ULDM models. These 93 galaxies have inclinations greater than 30° , have a measured value for the maximum circular velocity, V_f , in the SPARC catalog data, and have a quality flag that is not equal to three. A quality flag of three corresponds to galaxies with either of the three: major asymmetries, strong noncircular motions, or offsets between HI measurements and stellar distributions [10]. This generally means that the quoted measurements for the circular velocity may be unreliable. These galaxies also have a total number of circular velocity measurements greater than 11 (for galaxies without bulge components) or 12 (for galaxies with bulge components), which is the number of parameters in the double flavor, summed model.

The authors of [100] do consider multiple flavored models. However, for most of the galaxies analyzed, they perform fits assuming that each galactic structure is composed of a single species of ULDM, while each galactic structure could potentially be composed of a different ULDM species. They do, however, consider the MW to contain two solitonic structures composed of different ULDM species. We extend the results of this analysis by fitting more galaxies in the SPARC catalog to double flavor ULDM models, in which each galaxy is assumed to be composed of two solitonic structures made up of different ULDM species.

We also, in addition to treating each mass as a free parameter in the fitting procedure, scan over possible particle masses for each galaxy. In the next section, we further discuss the implications of treating each galactic structure as being composed of two species of ULDM. We note that our results may have been significantly different if we were to assume that each galaxy could be composed of either a single species or multiple species of ULDM and we leave an analysis of this sort for future work.

As opposed to some of the publications cited in this section, we do not assume that the SH relation is satisfied. Rather we check that this relation is satisfied after performing fits. Our reasoning is that the SH relation may be too restrictive, especially for some of the particle masses analyzed as well as for the double flavor models. We also choose to model the ULDM halo profile with the Einasto profile rather than the NFW or Burkert models. This is due, in part, to the fact that we find the Burkert and Einasto profiles to be the best performing CDM profiles analyzed in regards to the SPARC galaxies considered. The Einasto profile has also been shown to produce good fits to simulated halos of CDM over a large range of masses [11].

We extend the results of the studies cited in this section by analyzing both the reduced chi-square and BIC statistic of the resulting fits. While the reduced chi-square can be utilized to compare the ULDM and CDM models, the BIC statistic has a more conservative penalization of models with more parameters, and therefore penalizes the ULDM models (especially the double flavor models). We also extend previous studies by showing how the total sums of

the reduced chi-square values over all galaxies analyzed depend on the ULDM masses scanned. Finally, we show the resulting differences of the BIC statistics between the Einasto and ULDM models for the best fit particle masses found.

V. RESULTS

Here, we show some of the results for the ULDM models while more results for the ULDM and CDM models can be found in Appendix B. We show the results for ninety three galaxies in the SPARC catalog that have inclinations greater than 30° , have a measured value for the maximum circular velocity, V_f , in the SPARC catalog data, and have a quality flag that is not equal to three. These galaxies also have a total number of circular velocity measurements greater than 11 (for galaxies without bulge components) or 12 (for galaxies with bulge components), which is the number of parameters in the double flavor, summed model.

We start with the comparison of the ULDM models to the CDM models. We perform MLEs for the ULDM case in which particle mass is treated as a free parameter [ULDM models with (1) in Table I] and show results for the ULDM models using the Einasto profile as the halo profile. We compare this model to the Einasto only model as we find this and the Burkert model to perform better than the other CDM models analyzed (see Appendix B 2 b for results). We choose to compare the ULDM models to the Einasto model due to the theoretical justification from [11].

Figure 1 shows the difference in the BIC statistic between the Einasto model and each of the ULDM models ($\Delta\text{BIC} = \text{BIC}_{\text{Einasto}} - \text{BIC}_{\text{ULDM}}$) vs the particle mass. We also show the lines of $\Delta\text{BIC} = 0$, $|\Delta\text{BIC}| = 2$, $|\Delta\text{BIC}| = 6$, and $|\Delta\text{BIC}| = 10$ as the black dashed, blue, red, and green lines. The fraction of galaxies that fall within a particular range for ΔBIC is shown in the inset, where the Einasto model is always taken first in the difference. The points are shaded corresponding to the approximate probability density, with darker points corresponding to denser regions.

The top left panel of Fig. 1 shows ΔBIC for the single flavored ULDM model in which the ULDM soliton and halo are summed together [SS(1) model]. The largest fraction of galaxies (35%) shows a mild preference for the Einasto model, while the next largest fraction (30%) falls in the range of strong evidence in favor of the Einasto model. Therefore, well over half of the galaxies analyzed show a preference for the Einasto model. The next largest fraction (17%) falls in the range of decisive evidence for the SS(1) model, with the next largest fraction (10%) falling in the range of no preference for either model. This suggests that the Einasto model is, in general, a better fitting model than the SS(1) model when taking into account the penalization of more model parameters.

The middle and bottom panels (left column) of Fig. 1 show the double flavor model for which the soliton and

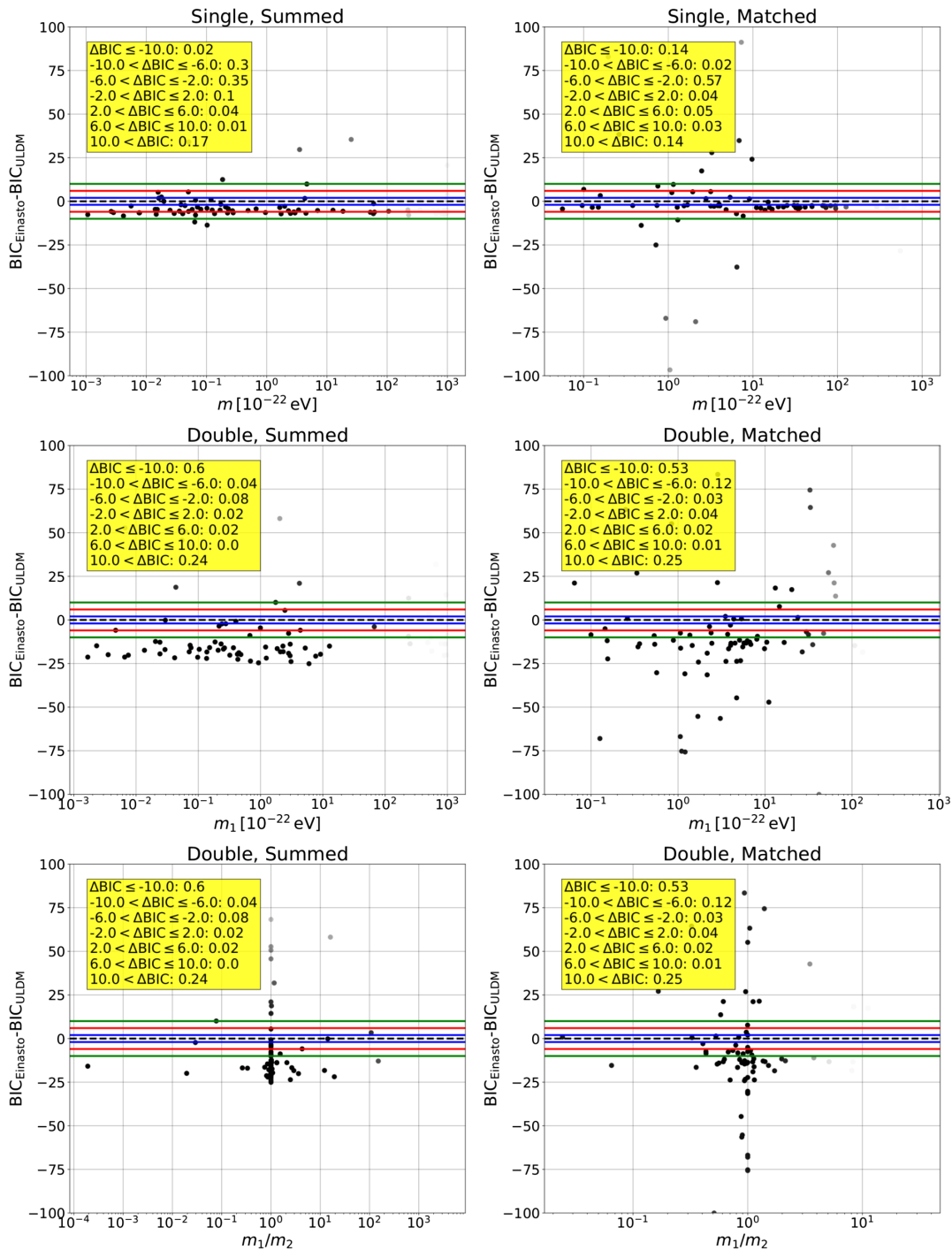


FIG. 1. Particle masses free—analysis (1) in Table I. Difference in the BIC statistics for Einasto and ULDM assuming the model: single flavor, profiles summed [SS(1)] (top left); single flavor, profiles matched [SM(1)] (top right); double flavor, profiles summed [DS(1)] (middle and bottom left); double flavor, profiles matched [DM(1)] (middle and bottom right). The middle panel corresponds to m_1 , and the bottom panel to m_1/m_2 . Black points correspond to each of the galaxies analyzed, the black dashed line corresponds to $\Delta BIC = 0$, blue lines correspond to $|\Delta BIC| = 2$, red lines to $|\Delta BIC| = 6$, and green lines to $|\Delta BIC| = 10$. Inset is the fraction of galaxies that fall within a given range for ΔBIC where the Einasto model is taken first in the difference. The points are shaded corresponding to the approximate probability density, with darker points corresponding to denser regions.

halo are summed [DS(1) model], with the middle panel corresponding to m_1 , and the bottom panel corresponding to m_1/m_2 . For this model, we obtain a large fraction (60%)

of the galaxies showing decisive evidence for the Einasto model, while a total of (72%) of galaxies show some preference to decisive evidence for the Einasto model.

A little less than a quarter of the galaxies (24%) show decisive evidence for the DS(1) model. Both summed models, then, result in most galaxies analyzed showing some preference to decisive evidence for the Einasto model, when more model parameters are penalized.

The right column of Fig. 1 shows the single and double flavor models for which the soliton and halo are matched [SM(1) and DM(1) models]. The SM(1) model performs better in some respects and worse in others than its summed counterpart [SS(1)], however the DM(1) model performs better overall than its summed counterpart [DS(1)]. This brings into question how the matched models would perform compared to the summed models if the matching relation [Eq. (2.15)] were relaxed, and we discuss this later.

Comparing the SM(1) model to the Einasto model, the largest fraction of galaxies (57%) falls in the range of mild preference for the Einasto model, with the next largest fractions (14%) being equal and with one showing decisive evidence for the SM(1) model and the other showing decisive evidence for the Einasto model. Comparing the

DM(1) model to the Einasto model, a little over half of the galaxies (53%) show decisive evidence for the Einasto model, and a quarter of the galaxies (25%) show decisive evidence for the DM(1) model. The next largest fraction (12%) shows strong evidence for the Einasto model.

It is interesting to point out here that even though we let the particle masses vary in the range $10^{-3}m_{22} \leq m \leq 10^3m_{22}$, for the matched models almost all galaxy fits prefer particle masses within the bounds of $10^{-1}m_{22} \lesssim m \lesssim 10^2$. We explore this range of masses in more detail when we fix the particle masses in the fitting procedure. Also, for the double flavored models, almost all galaxy fits prefer particle mass ratios in the range $10^{-2} \lesssim m_1/m_2 \lesssim 10$, with most galaxies showing a preference for approximately equal particle masses.

In our fitting procedure for the double flavor models, we take the initial guess for both of the soliton and particle masses to be equal. The fact that the best fit parameters for both the particle masses happen to be approximately equal for many galaxies suggest that the choice of particle mass has

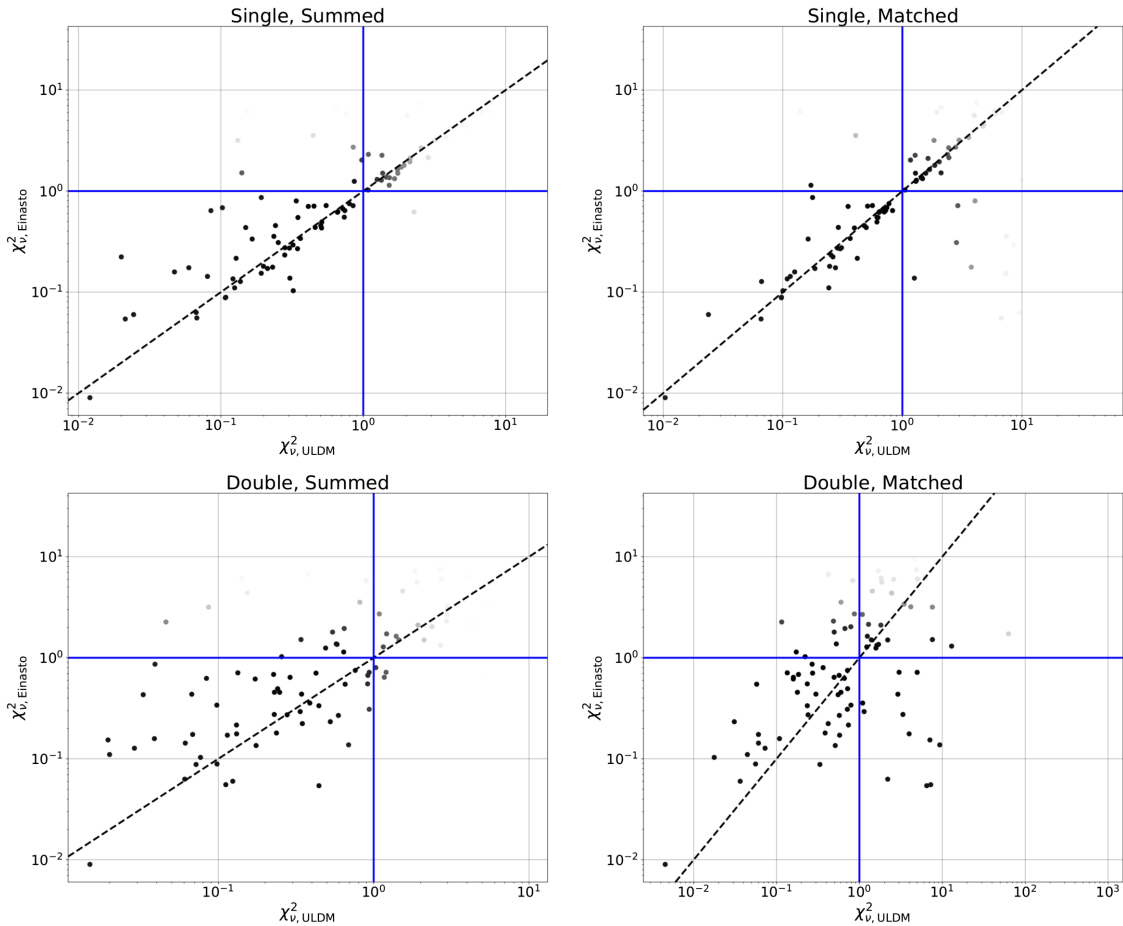


FIG. 2. Particle masses free—analysis (1) in Table I. Reduced chi-square for the Einasto model vs reduced chi-square for the ULDM models: SS(1) (top left); SM(1) (top right); DS(1) (bottom left); DM(1) (bottom right). The black dashed lines correspond to $\chi^2_{\nu, \text{Einasto}} = \chi^2_{\nu, \text{ULDM}}$ while the blue horizontal lines show where $\chi^2_{\nu, \text{Einasto}} = 1$ and the blue vertical lines show where $\chi^2_{\nu, \text{ULDM}} = 1$. The points are shaded corresponding to the approximate probability density, with darker points corresponding to denser regions.

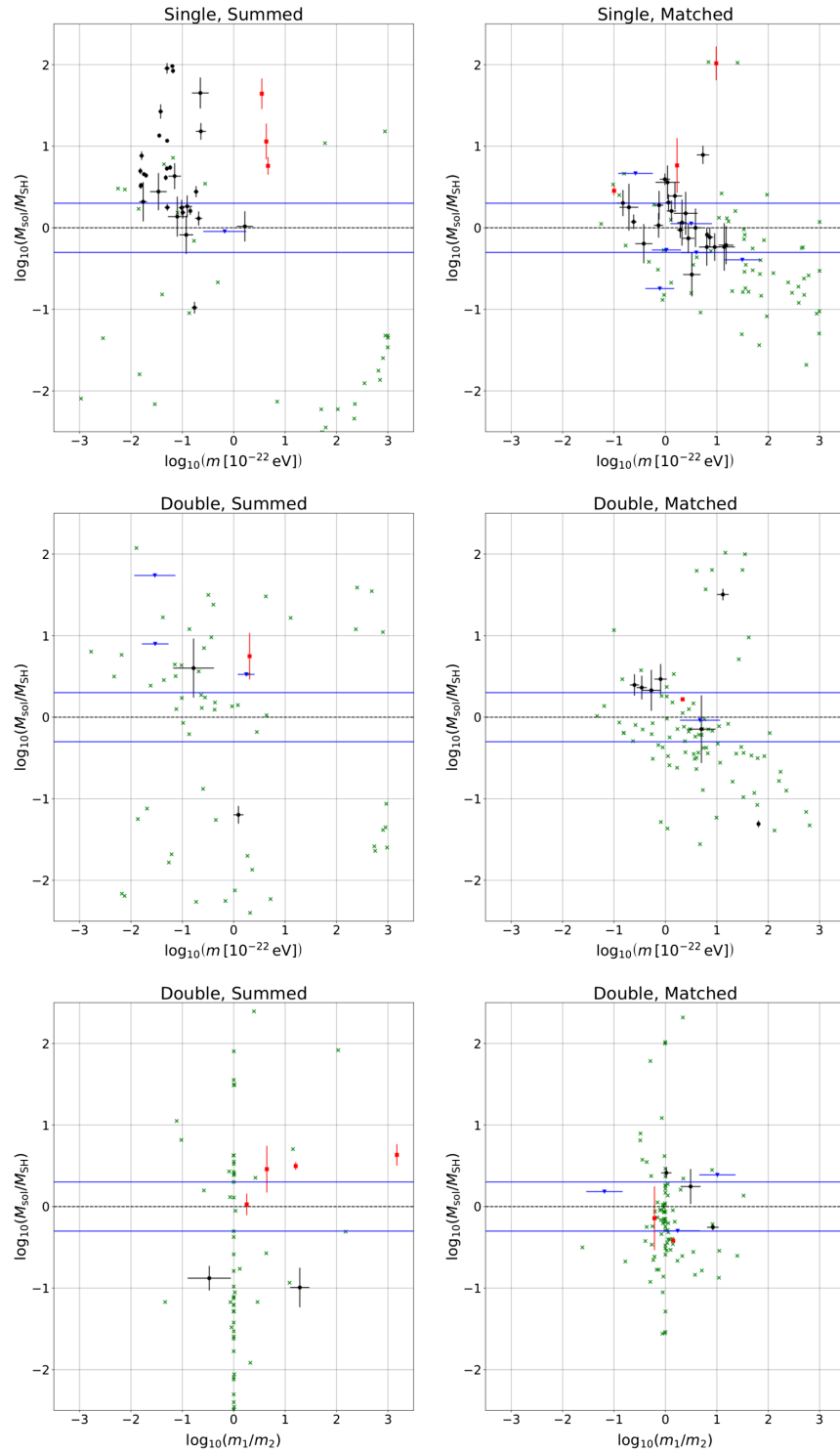


FIG. 3. Particle masses free—analysis (1) in Table I. $\log_{10}(M_{\text{sol}}/M_{\text{sol,SH}})$ vs $\log_{10} m$ where $M_{\text{sol,SH}}$ refers to the soliton mass assuming the SH relation given by Eq. (2.18) for the assumed models: SS(1) (top left), SM(1) (top right), DS(1) (middle and bottom left), and DM(1) (middle and bottom right) with the middle row corresponding to m_1 and the bottom to m_1/m_2 . We plot each galaxy with a given marker depending on the error measurements for the particle and soliton masses. The error calculated can either be (–) nonexistent or larger than the best fit parameter or (+) smaller than the best fit parameter. Black points correspond to galaxies with (+) for both the soliton and particle mass; red squares correspond to galaxies with (+) for the soliton mass and (–) for the particle mass; blue triangles correspond to galaxies with (–) for the soliton mass and (+) for the particle mass; green Xs correspond to galaxies with (–) for both the soliton and particle masses.

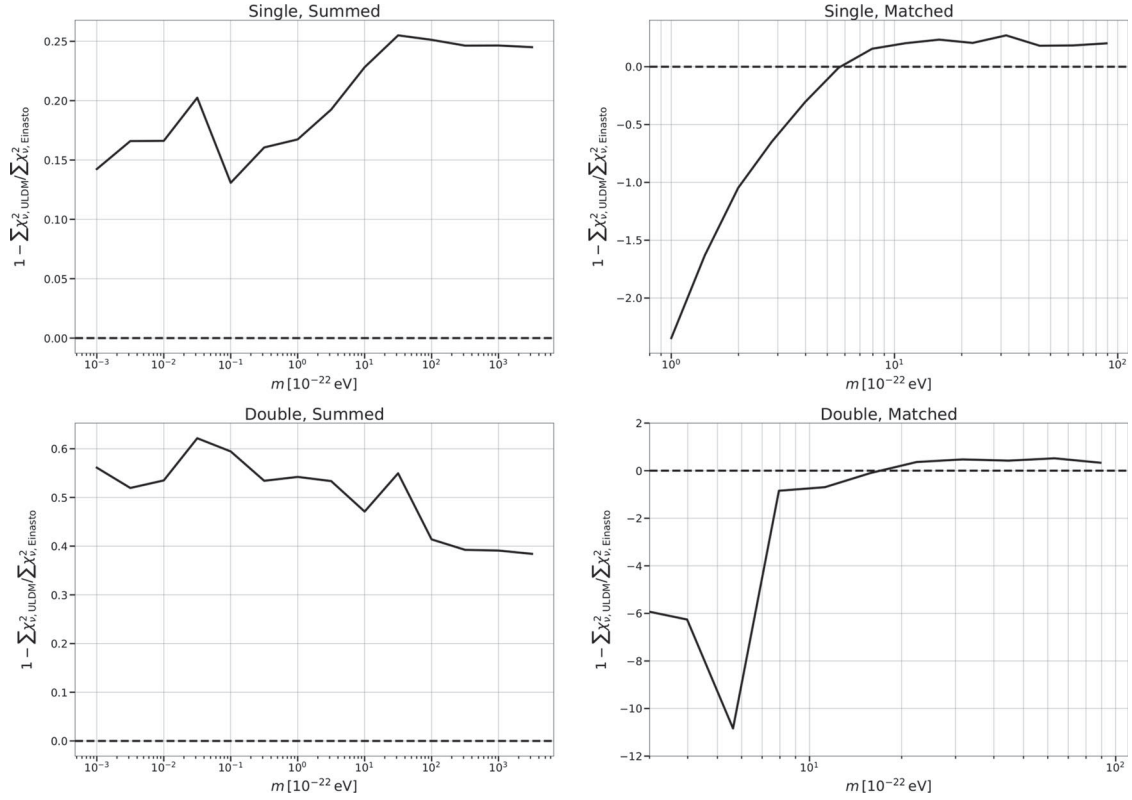


FIG. 4. Particle masses fixed and scanned—analysis (2) in Table I. $f(\chi^2) \equiv 1 - \sum \chi_{\nu, \text{ULDM}}^2 / \sum \chi_{\nu, \text{Einasto}}^2$ vs particle mass for the assumed models: SS(2) (top left), SM(2) (top right), DS(2) (bottom left), and DM(2) (bottom right).

little effect on the maximum likelihood estimates. This is a reasonable suggestion, as the presence of the soliton will effect only the innermost regions, on the order of a kpc or less, where many galaxies have less data points. We discuss this further when we discuss the error estimates for the best fit parameters.

We now turn to the reduced chi-square statistic which does not penalize more model parameters as much as the BIC statistic. Figure 2 shows the reduced chi-square for the Einasto model vs the reduced chi-square for each of the ULDM models. The top left panel shows the SS(1) model, which has a significant number of galaxies giving reduced chi-square values for the Einasto model closer to one. The top right panel shows the SM(1) model, which has a tighter correlation with $\chi_{\nu, \text{Einasto}}^2 = \chi_{\nu, \text{ULDM}}^2$ than its summed counterpart. The bottom left panel shows the DS(1) model, while the bottom right panel shows the DM(1) model. In both cases, many galaxies give reduced chi-square values for the Einasto model that are closer to one. For the matched model, many galaxies give reduced chi-square values greater than one, with some being significantly greater than one.

We now check the SH halo relation given by Eq. (2.18). We compare the fit result soliton mass, M_{sol} , obtained in each ULDM model to the soliton mass as given by the SH relation, denoted as $M_{\text{sol,SH}}$. For both the summed and matched models, the fit result soliton mass is the resulting

best fit parameter. Figure 3 shows the ratio (in log-10 space) between M_{sol} and $M_{\text{sol,SH}}$ vs particle mass. The top row shows the single flavored model with the summed model [SS(1)] along the left column and the matched model [SM(1)] along the right column while the middle and bottom row correspond to the double flavored models [DS(1) on the left and DM(1) on the right]. The middle row corresponds to m_1 , and the bottom row corresponds to m_1/m_2 . The blue lines allow for letting the SH relation differ by a factor of 2.

The galaxies are marked with different markers depending on the error calculated in the fitting procedure, which we categorize as (−) error measurements that are non-existent or larger than the best fit parameter; or (+) error measurements that are smaller than the best fit parameter. Black points have (+) for both the soliton and particle masses; red squares have (+) for the soliton mass and (−) for the particle mass; blue triangles have (−) for the soliton mass and (+) for the particle mass; and green Xs have (−) for both the soliton and particle masses.

For the summed models (left panel of Fig. 3), there does not seem to be any trend of galaxies following the SH relation, while for the double flavor models, we obtain poor error measurements for many of the galaxies. For the matched models (right panel), there is a tighter correlation with the SH relation, while the double flavor models again give many galaxies with poor error measurements.

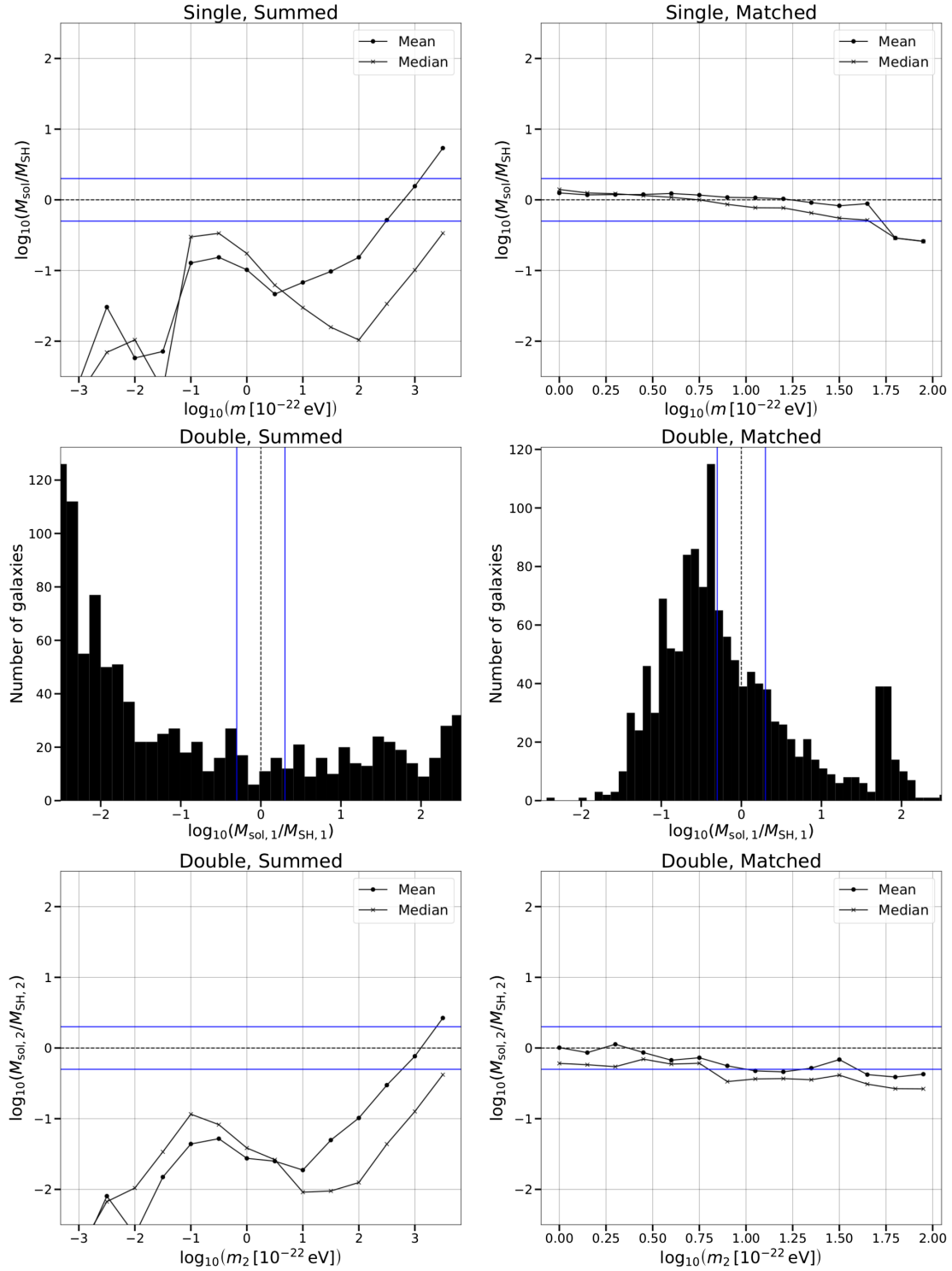


FIG. 5. Particle masses fixed and scanned—analysis (2) in Table I. $\log_{10}(M_{\text{sol}}/M_{\text{sol,SH}})$ vs $\log_{10} m$ (top and bottom panels) where $M_{\text{sol,SH}}$ refers to the soliton mass assuming the SH relation given by Eq. (2.18). The top row corresponds to the SS(2) (left) and SM(2) (right) models. The middle and bottom rows correspond to the DS(2) (left) and DM(2) (right) models. The middle row corresponds to the particle mass fixed at $m = 10^{1.5}m_{22}$ and shows the histogram of $\log_{10}(M_{\text{sol},1}/M_{\text{SH},1})$ for this particular mass. The bottom row corresponds to the particle mass that is varied in the double flavor models. For the top and bottom rows, the black points (Xs) correspond to the mean (median) value of $\log_{10}(M_{\text{sol}}/M_{\text{sol,SH}})$.

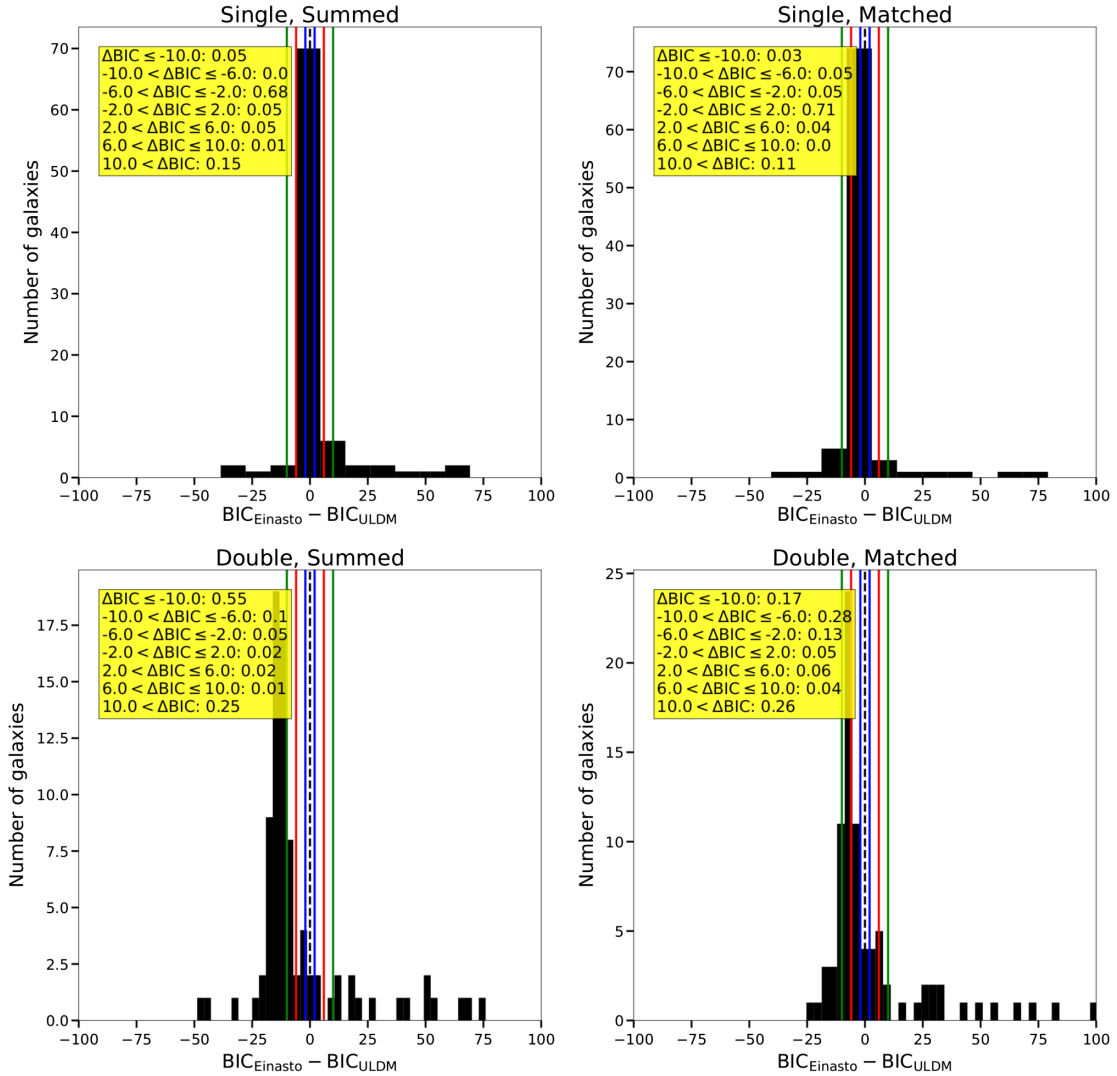


FIG. 6. Particle masses fixed ($m_1 = 10^{1.5}m_{22}$, $m_2 = 10^{1.8}m_{22}$). Difference in the BIC statistics for Einasto and ULDM assuming the model: SS (top left), SM (top right), DS (bottom left), DM (bottom right). The black dashed line corresponds to $\Delta\text{BIC} = 0$, blue lines correspond to $|\Delta\text{BIC}| = 2$, red lines to $|\Delta\text{BIC}| = 6$, and green lines to $|\Delta\text{BIC}| = 10$. Inset is the fraction of galaxies that fall within a given range for ΔBIC where the Einasto model is taken first in the difference.

Building on the suggestion above in regards to the fitting procedure choosing approximately equal particle masses for the double flavor model, the fact that many galaxies give poor error estimates further confirms the suggestion that the MLEs are largely unaffected by changes in the soliton and particle masses.

Treating the particle mass as free in the fitting procedure suggests the lack of any preference for a particular range of particle masses, within the range of masses searched, for the summed models. However, for the DS(1) model, there is a significant preference for particle masses that are approximately equal. For the matched models, on the other hand, there does seem to be a preference for a range of particle masses $m_{22} \lesssim m \lesssim 10^2$. We, therefore, scan this mass range when we treat the particle masses as fixed parameters. As in the summed model, there also seems to

be a preference for approximately equal masses for the DM(1) model.

We now discuss the ULDM models when the particle mass is fixed and scanned in the fitting procedure [ULDM models with (2) in Table I]. Figure 4 shows $f(\chi^2_\nu) \equiv 1 - \sum \chi^2_{\nu, \text{ULDM}} / \sum \chi^2_{\nu, \text{Einasto}}$ vs fixed particle mass, where the sum is taken over all galaxies analyzed. The single flavored models are shown on the top row with the summed model along the left column [SS(2)] and the matched model along the right column [SM(2)]. The double flavored models are shown on the bottom row [DS(2) on the left and DM(2) on the right].

We find that the SS(2) model (top left panel of Fig. 4) differs from the Einasto model by at most approximately 25% and gives $f(\chi^2_\nu) > 0$ for all masses scanned. The SM(2) model, on the other hand, differs more for masses

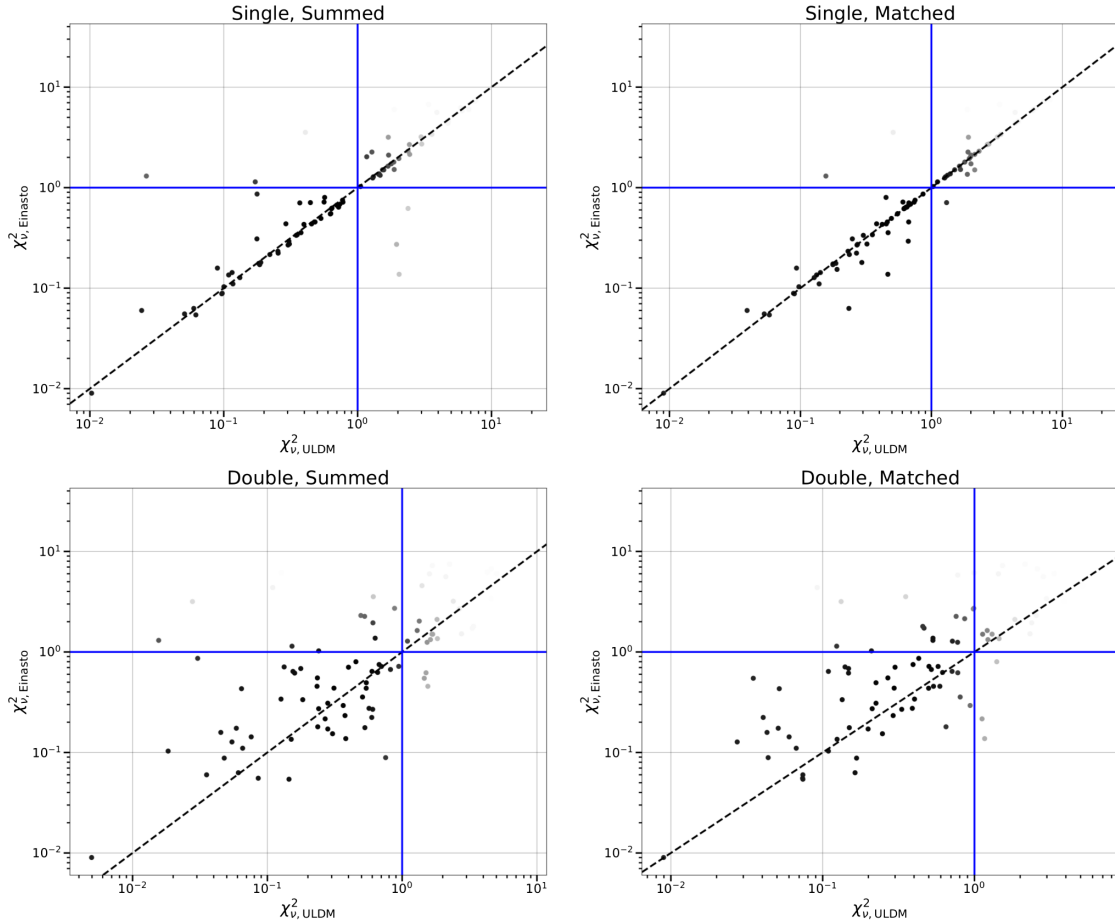


FIG. 7. Particle masses fixed ($m_1 = 10^{1.5}m_{22}$, $m_2 = 10^{1.8}m_{22}$). Reduced chi-square for the Einasto model vs reduced chi-square for the ULDM models: SS (top left), SM (top right), DS (bottom left), DM (bottom right). The black dashed lines correspond to $\chi^2_{\nu, \text{Einasto}} = \chi^2_{\nu, \text{ULDM}}$ while the blue horizontal lines show where $\chi^2_{\nu, \text{Einasto}} = 1$ and the blue vertical lines show where $\chi^2_{\nu, \text{ULDM}} = 1$. The points are shaded corresponding to the approximate probability density, with darker points corresponding to denser regions.

$m \lesssim 3m_{22}$. All masses scanned in the range $6m_{22} \lesssim m \lesssim 10^2m_{22}$ give $f(\chi^2_\nu) > 0$. For both the SS(2) and SM(2) models, we find the best fit mass to be $m = 10^{1.5}m_{22}$. We then fix one of the particle masses to this particular particle mass when analyzing the double flavor models [DS(2) and DM(2)].

The bottom row of Fig. 4 shows the double flavor models for which one of the particle masses is fixed to $m_1 = 10^{1.5}m_{22}$, and the other is scanned over a particular range (see Table I for ranges). The bottom left panel shows the DS (2) model which gives $f(\chi^2_\nu) > 0$ for all masses scanned. This model differs from the Einasto model by at most approximately 60% and by at least approximately 40%. The DM(2) model, on the other hand, differs from the Einasto model significantly for masses $m_2 \lesssim 10m_{22}$. The DM(2) model gives $f(\chi^2_\nu) > 0$ for masses $11m_{22} \lesssim m_2 \lesssim 10^2m_{22}$, and gives the best results for masses $m_1 = 10^{1.5}m_{22}$ and $m_2 = 10^{1.8}m_{22}$. Later, we show some results assuming these fixed masses.

The results discussed above are obtained with no dependence on the SH relation. We now show how the results compare to this relation given by Eq. (2.18). As in the analysis case for which the particle mass was free to vary in the fitting procedure, we compare the fit result soliton mass, M_{sol} , to the soliton mass as given by the SH relation, $M_{\text{sol,SH}}$. Figure 5 shows the ratio (in log-10 space) of M_{sol} to $M_{\text{sol,SH}}$ vs the particle mass for the top and bottom rows. Black points (Xs) correspond to the mean (median) value of $\log_{10}(M_{\text{sol}}/M_{\text{sol,SH}})$. The middle row shows the distribution of $\log_{10}(M_{\text{sol}}/M_{\text{sol,SH}})$ for the fixed particle mass $m_1 = 10^{1.5}m_{22}$ for the double flavor model. The number of samples corresponds to the number of galaxies analyzed for each possible m_1, m_2 pair, with m_2 varied along the same range as in the single flavored model.

The top row shows the single flavored models, with the SS(2) model on the left and SM(2) model on the right. The SS(2) model gives both the mean and median outside of the SH relation range for almost all particle masses scanned,

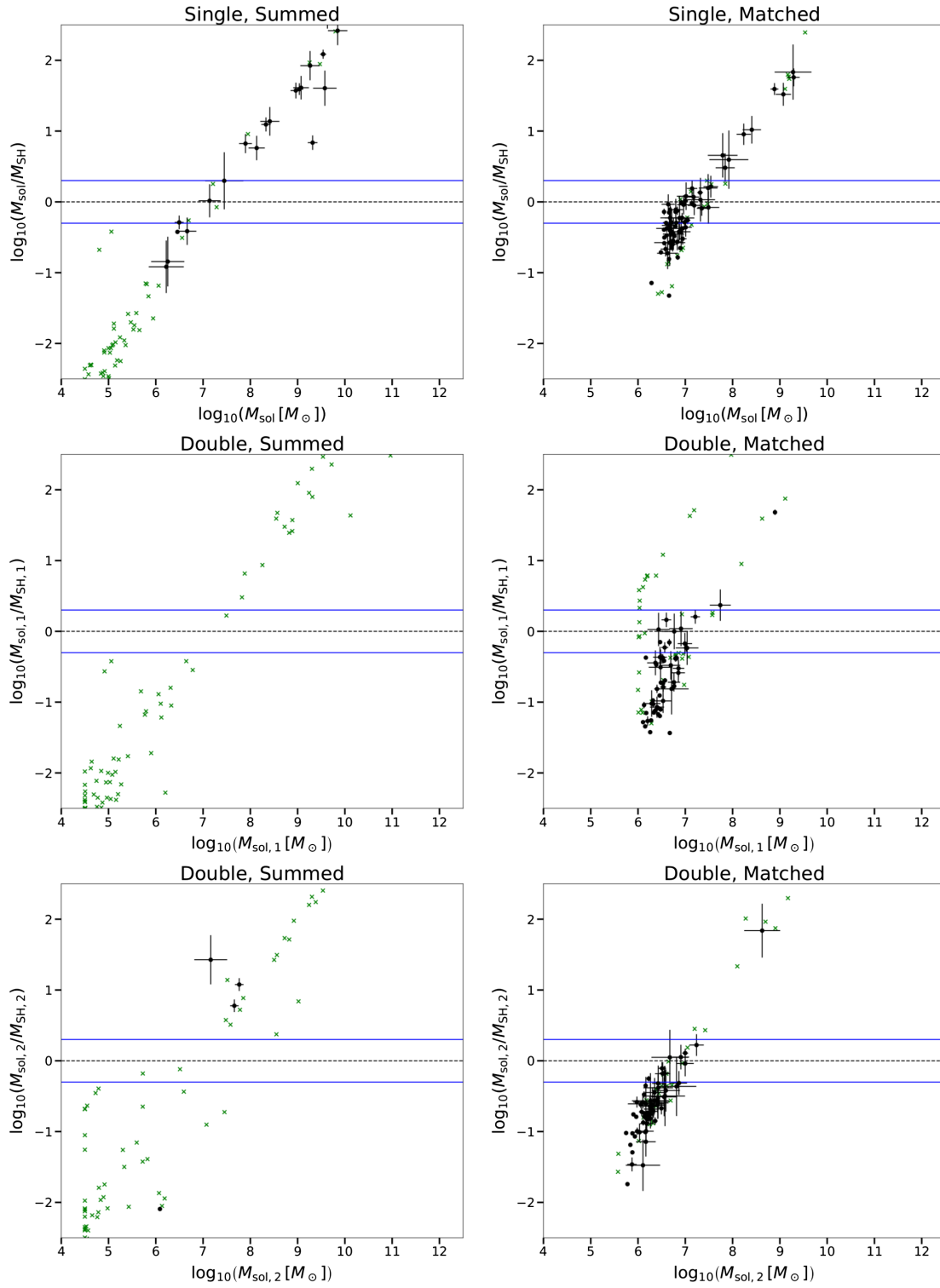


FIG. 8. Particle masses fixed ($m_1 = 10^{1.5}m_{22}$, $m_2 = 10^{1.8}m_{22}$). $M_{\text{sol}}/M_{\text{sol,SH}}$ where $M_{\text{sol,SH}}$ refers to the soliton mass assuming the soliton halo relation given by Eq. (2.18). The top row corresponds to the SS (left) and SM (right) models. The middle and bottom rows correspond to the DS (left) and DM (right) models. The top and middle row corresponds to the particle mass fixed at $m = 10^{1.5}m_{22}$, and the bottom row to the particle mass fixed at $m = 10^{1.8}m_{22}$. The points are marked in the same way as in Fig. 3.

while the SM(2) model results in almost all masses scanned giving the mean and median values falling within the SH relation range. We see the same sort of behavior for double flavor models.

Finally, we fix the particle masses to $m_1 = 10^{1.5}m_{22}$ for all ULDM models and $m_2 = 10^{1.8}m_{22}$ for the double flavor models and vary all the rest of the parameters as in analysis (2) in Table I. Figure 6 shows $\Delta\text{BIC} = \text{BIC}_{\text{Einasto}} - \text{BIC}_{\text{ULDM}}$ for the SS (top left), SM (top right), DS (bottom left), and DM (bottom right) models. Comparing this to Fig. 1, one can see that all models besides the DS model perform better when the masses are fixed in this way rather than being allowed to vary in the fitting procedure, with the matched models performing significantly better.

We can also compare the reduced chi-square results to those for which the particle mass is allowed to vary in the fitting procedure (Fig. 2). Figure 7 shows the reduced chi-square for the Einasto model vs the reduced chi-square for the ULDM models, again fixing the particle masses to $m_1 = 10^{1.5}m_{22}$ and $m_2 = 10^{1.8}m_{22}$. Both the SS (top left) and SM (top right) models have most galaxies tightly correlated with $\chi_{\nu, \text{Einasto}}^2 = \chi_{\nu, \text{ULDM}}^2$, with the matched model giving a handful of galaxies that result in a reduced chi-square closer to one than the Einasto model. The DS (bottom left) model performs a bit better than the case in which the particle masses are allowed to vary, with more galaxies giving a reduced chi-square closer to one than the Einasto model. The DM (bottom right) model performs significantly better than the case in which the particle masses are allowed to vary, with most galaxies that gave significantly large reduced chi-squares now giving reduced chi-squares closer to one.

Finally, we show how the resulting soliton masses compare to the SH relation in Fig. 8 when the particle masses are fixed to $m_1 = 10^{1.5}m_{22}$ and $m_2 = 10^{1.8}m_{22}$. These results can be compared to the case in which the particle mass is allowed to vary (Fig. 3) and the case in which the particle masses are fixed, but scanned in the fitting procedure (Fig. 5). The points are marked in the same way as in Fig. 3. When the particle masses are fixed in this way, we find that again the summed models have a larger variance with respect the SH relation compared to the matched model, while we again find many galaxies giving poor error measurements for the double flavor summed model. On the other hand, the double flavor matched model gives significantly more galaxies with reasonable error measurements calculated in the fitting procedure [compared to the DM(1) analysis]. This suggests that when the particle masses are fixed in this way, the MLEs have a larger dependence on the soliton mass.

We refer the reader to Appendix B for many more results. We include the comparisons with other empirical relations (i.e., the CMR, BTFR, AMR, and gravitational RAR), statistical and parameter distributions for all models analyzed, and various rotation curves. We also note that some

galaxies exhibit a strong degeneracy in the best fit values for \tilde{Y}_d . In this case, it is possible for the fitting routine to choose best fit values for \tilde{Y}_d that are at the minimum or maximum values.

VI. CONCLUSION

We compared single and double flavor ULDM models of galactic dark matter to each other and to commonly used CDM models. We fit these models to the measured galactic circular velocities of galaxies in the SPARC catalog, and compare models using the reduced chi-square and BIC statistics. We analyzed cases for which the particle masses in the ULDM models are free to vary, and for which the particle masses are fixed in the fitting procedure. For each of these analyses, we perform fits for ULDM models in which the soliton and halo are summed together; and for ULDM models in which the soliton and halo are matched.

When the particle mass was free in the fitting procedure, we found that there is a negligible preference for any particular range of particle masses, within $10^{-25} \text{ eV} \leq m \leq 10^{-19} \text{ eV}$, when assuming the summed models. For the matched models, however, we found that almost all galaxies prefer particles masses in the range $10^{-23} \text{ eV} \lesssim m \lesssim 10^{-20} \text{ eV}$. For both double flavor models (summed and matched) we found that most galaxies prefer approximately equal particle masses.

When the particle masses were fixed in the fitting procedure, we found that both single flavor models gave a maximum in $f(\chi_{\nu}^2) \equiv 1 - \sum \chi_{\nu, \text{ULDM}}^2 / \sum \chi_{\nu, \text{Einasto}}^2$, where the sum is taken over all galaxies, for the particle mass $m = 10^{-20.5} \text{ eV}$. The single flavor, summed models gave $f(\chi_{\nu}^2) > 0$ for all masses scanned, while the single flavor, matched model gave $f(\chi_{\nu}^2) > 0$ for all masses scanned in the range $6 \times 10^{-22} \text{ eV} \lesssim m \lesssim 10^{-20} \text{ eV}$. For the double flavor models, we fixed one of the particle masses to the best fit particle mass $m_1 = 10^{-20.5} \text{ eV}$. The double flavor, summed model gave $f(\chi_{\nu}^2) > 0$ for all masses scanned, while the double flavor, matched model gave $f(\chi_{\nu}^2) > 0$ for masses $11 \times 10^{-22} \text{ eV} \lesssim m_2 \lesssim 10^{-20} \text{ eV}$. The double flavor, matched model gave the best fit results for masses $m_1 = 10^{-20.5} \text{ eV}$ and $m_2 = 10^{-20.2} \text{ eV}$.

The results shown in this study were based on different assumptions that can be changed. First, it is important to note that one can treat the point at which the soliton and halo are matched as a free parameter. It is also possible to take into account the fact that some galaxies may be better fit by a single flavor, and some to a double flavored model, while each galaxy could have differing radii at which the soliton and halo are matched. Finally, one can also fit each galaxy based on the fit parameters of the last galaxies, a problem that can be handled particularly well using reinforcement learning. In this case, one may find a set of parameters that better fit more galaxies on average.

These possibilities result in a complex map of ULDM halos dependent on the abundance of the ULDM species and the collapse history of the ULDM halo. We discuss these possibilities in a future study in which we utilize a reinforcement learning algorithm to take into account the complex map of possibilities and infer the possible ULDM abundances present today.

ACKNOWLEDGMENTS

This material is based upon work supported by the U.S. Department of Energy (DOE), Office of Science, Office of Workforce Development for Teachers and Scientists, Office of Science Graduate Student Research (SCGSR) program. The SCGSR program is administered by the Oak Ridge Institute for Science and Education (ORISE) for the DOE. ORISE is managed by ORAU under Contract No. DE-SC0014664. All opinions expressed in this paper are the authors' and do not necessarily reflect the policies and views of DOE, ORAU, or ORISE. L. S. thanks Joshua Eby and Peter Suranyi for valuable discussions. L. S. thanks Mike Sokoloff and Daniel Vieira for setting up computational resources to be used in the next installment of this study.

APPENDIX A: RELATIONS

For all analyses, we check that the distribution of mass-to-light ratios is consistent with stellar synthesis models [39], that the resulting stellar and halo masses fit the AMR [36,37], that the baryonic mass and maximum circular velocity fit the BTFR [38], that the gravitational acceleration due to baryons and that due to DM fit the gravitational RAR of [40], and that the CMR [11,35] is reproduced. For the ULDM models, we also check that the SH relation [Eq. (2.18)] is reproduced.

The RAR of [40] is given by

$$g_{\text{tot}}(r) = g_{\text{bar}} \left(1 - e^{-\sqrt{g_{\text{bar}}(r)/g_{\ddagger}}} \right)^{-1}, \quad (\text{A1})$$

where g_{tot} is the total gravitational acceleration and g_{bar} is that due to baryons at a given radial distance r and g_{\ddagger} was fit to be $g_{\ddagger} = 1.2 \times 10^{-10} \text{ m/s}^2$.

The concentration mass relation of [35] is given by

$$\log_{10} c_{200} = 0.905 - 0.101 \log_{10} \left(\frac{M_{200}}{10^{12} h^{-1} M_{\odot}} \right), \quad (\text{A2})$$

with a scatter of 0.11 dex. The concentration mass relation of [11] is given by

$$c_{200} = \sum_{i=0}^5 c_i \ln \left(\frac{M_{200}}{h^{-1} M_{\odot}} \right), \quad (\text{A3})$$

where $c_i = [27.112, -0.381, -1.853 \times 10^{-3}, -4.141 \times 10^{-4}, -4.334 \times 10^{-6}, 3.208 \times 10^{-7}]$ for $i \in \{0, 5\}$.

The baryonic Tully-Fisher relation of [38] is given by

$$\log_{10} \left(\frac{M_b}{M_{\odot}} \right) = s \log_{10} \left(\frac{V_f}{\text{km/s}} \right) + \log_{10} A, \quad (\text{A4})$$

where M_b is the baryonic mass, V_f is the maximum circular velocity, and the fit parameters were found to be $s = 3.71 \pm 0.08$ and $\log_{10} A = 2.27 \pm 0.18$.

Finally, the abundance matching relation between stellar and DM masses is given by [36,37]

$$\frac{M_*}{M_{200}} = 2N \left[\left(\frac{M_{200}}{M_1 M_{\odot}} \right)^{-\beta} + \left(\frac{M_{200}}{M_1 M_{\odot}} \right)^{-\gamma} \right]^{-1}, \quad (\text{A5})$$

where M_* is the total stellar mass, M_{200} is the DM halo mass, $N = 0.0351$, $\beta = 1.376$, $\gamma = 0.608$, and $\log_{10}(M_1) = 11.59$.

APPENDIX B: RESULTS

Here, we show many more results including the single and ULDM models (Appendix B 1), a comparison with previous studies (Appendix B 2 a), and results for the CDM models (Appendix B 2 b).

1. ULDM

We now show more results for which the particle masses are fixed to $m_1 = 10^{1.5} m_{22}$ and $m_2 = 10^{1.8} m_{22}$, which gave the best fitting results for the galaxies analyzed. For the main results see Sec. V (Figs. 6, 7, and 8):

- (i) Figure 9 shows the reduced chi-square values.
- (ii) Figure 10 shows some of the parameter distributions. The second from the bottom and bottom rows show the distributions of $\tilde{\Upsilon}_d$ and $\tilde{\Upsilon}_b$, respectively. Both distributions tend to peak near the lower boundary of 0.01.
- (iii) Figure 11 shows rotation curves for the galaxies NGC5055 and NGC3109 for the summed models.
- (iv) Figure 12 shows rotation curves for the galaxies NGC5055 and NGC3109 for the matched models.
- (v) Figure 13 shows the empirical relations analyzed (the gravitational RAR of [40], the CMR [11,35], the BTFR [38], and the AMR [36,37]). For the gravitation RAR, all ULDM models give a value of g_{\ddagger} that is close to the MOND value. All models tend to give significant scatter around both CMR relations, around the BTFR relation, and around the AMR relation, with less scatter around the BTFR relation.

We also show more results for which the particle mass is free to vary in the fitting procedure. For the main results see Sec. V (Figs. 1, 2, and 3):

- (i) Figure 14 shows the reduced chi-square values.

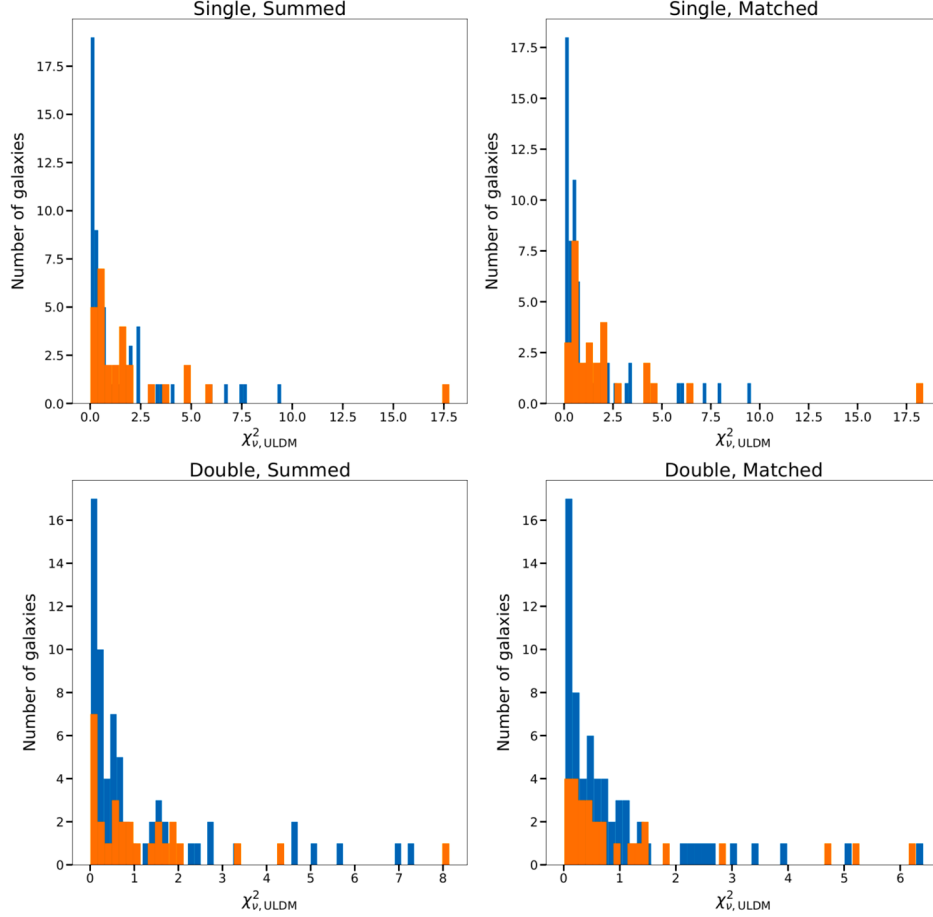


FIG. 9. Particle masses fixed ($m_1 = 10^{1.5}m_{22}$, $m_2 = 10^{1.8}m_{22}$). Reduced chi-square χ^2_v for the assumed models: single, summed (top, left); single, matched (top, right); double, summed (bottom, left); double, matched (bottom, right).

- (ii) Figure 15 shows some of the parameter distributions. The second from the bottom and bottom rows show the distributions of $\tilde{\Upsilon}_d$ and $\tilde{\Upsilon}_b$, respectively. As in Fig. 10 both distributions tend to peak near the lower boundary of 0.01.
- (iii) Figure 16 shows rotation curves for the galaxies NGC5055 and NGC3109 for the summed models.
- (iv) Figure 17 shows rotation curves for the galaxies NGC5055 and NGC3109 for the matched models.
- (v) Figure 18 shows the empirical relations analyzed (the gravitational RAR of [40], the CMR [11,35], the BTFR [38], and the AMR [36,37]). As in Fig. 13, all ULDM models give a value of g^\dagger that is close to the MOND value. All models tend to give significant scatter around both CMR relations, around the BTFR relation, and around the AMR relation, with less scatter around the BTFR relation.

2. CDM

a. Comparison with previous CDM studies

First, we discuss the reproduction of results from previous studies. Similarly to [24], we compare the NFW and DC14

profile fits for the SPARC galaxies. Here, we take only galaxies with inclinations greater than 30° , and we omit galaxies with quality flags equal to 3. This leaves us with 149 galaxies analyzed, rather than the 147 galaxies analyzed in [24]. We compare our results to the flat prior analysis of [24], where the free parameters are constrained to the ranges $1 \leq c_{200} \leq 100$, $10 \leq V_{200} \leq 500$, $0.3 \leq \tilde{\Upsilon}_d \leq 0.8$, and $0.3 \leq \tilde{\Upsilon}_b \leq 0.8$. Finally, we also take the constraint $(M_* + M_{\text{gas}})/M_{\text{DM}} < 0.2$ as in [24].

With this analysis set up, we confirm that the DC14 profile better fits more galaxies analyzed. We are able to approximately reproduce Fig. 1 of [24] as well as the rotation curves of Figs. A1–A7 for the flat prior case. We obtain the median reduced chi-squared [Eq. (3.4)] for all galaxies to be $\chi^2_{v,\text{NFW}} \approx 1.55$ and $\chi^2_{v,\text{DC14}} \approx 0.85$. We also obtain the following fraction of galaxies, f , with $\Delta\text{BIC} = \text{BIC}_{\text{NFW}} - \text{BIC}_{\text{DC14}}$: $f = 0.36$ for $\Delta\text{BIC} > 6$; $f = 0.13$ for $6 \geq \Delta\text{BIC} > 2$; $f = 0.28$ for $2 \geq \Delta\text{BIC} > -2$; $f = 0.05$ for $-2 \geq \Delta\text{BIC} > -6$; and $f = 0.17$ for $-6 \geq \Delta\text{BIC}$.

Next, we discuss the reproduction of results from [26]. Here, we analyze all 175 galaxies, take uniform priors, and constrain the ranges of parameters to be $1 \leq c_{200} \leq 1000$,

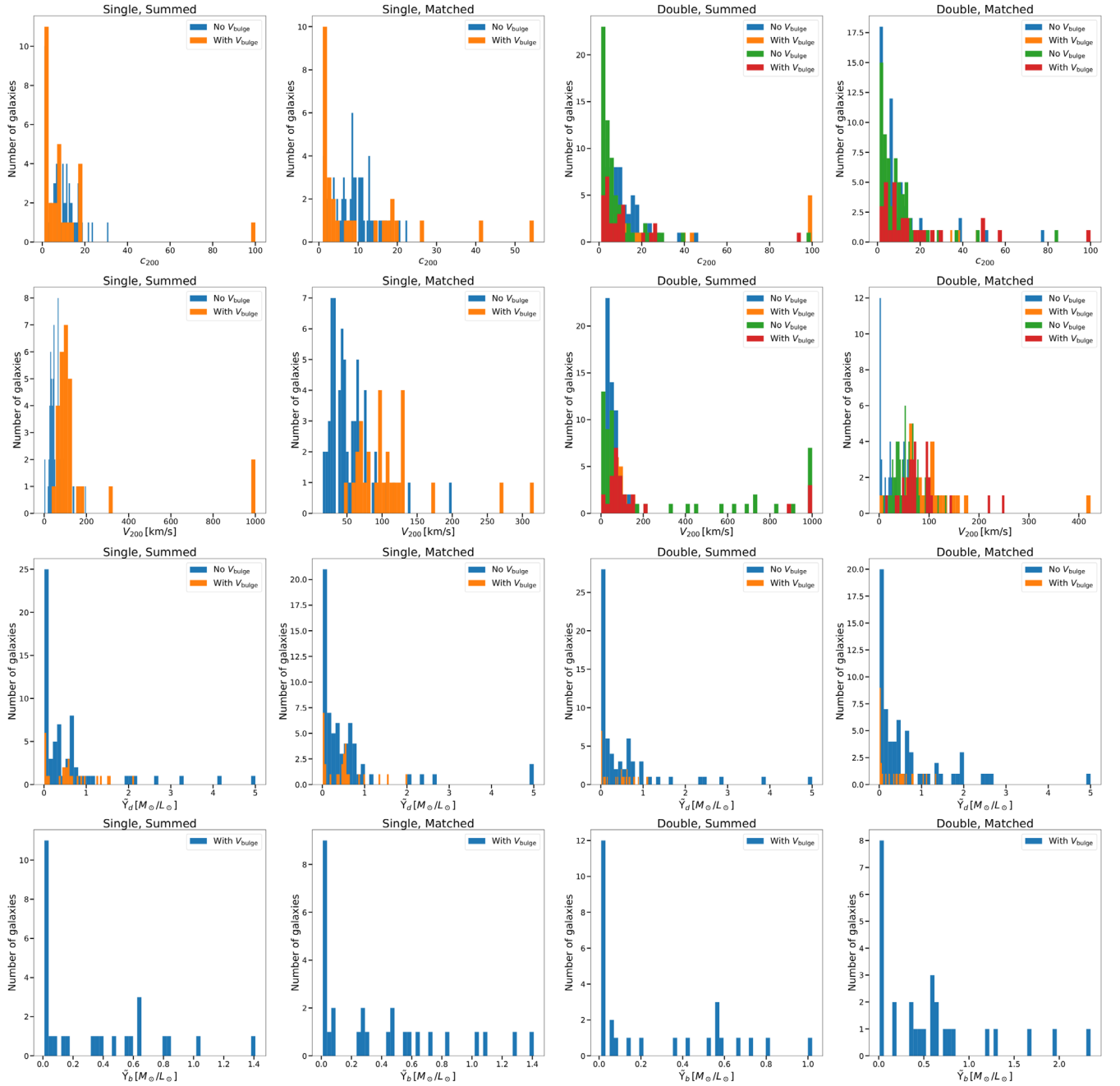


FIG. 10. Particle masses fixed ($m_1 = 10^{1.5} m_{22}$, $m_2 = 10^{1.8} m_{22}$). Distributions for c_{200} (top row), V_{200} (second from top row), $\tilde{\Upsilon}_d$ (third from top row), and $\tilde{\Upsilon}_b$ (bottom row) for the single, summed (left column), single, matched (second column from the left), double, summed (third column from the left), and double, matched (right column) models.

$10 \leq V_{200} \leq 500$, $0.01 \leq \tilde{\Upsilon}_d \leq 5$, $0.01 \leq \tilde{\Upsilon}_b \leq 5$, and $5 \times 10^{-3} \leq \alpha \leq 5$. We are able to approximately reproduce Fig. 1 and the rotation curve plots for a handful of galaxies (for the Burkert, DC14, Einasto, and NFW profiles). However, we obtain differing results for the free parameters, especially the mass-to-light ratios (which we take to have uniform rather than log-normal priors).

We also find that many galaxies have a strong degeneracy in the best fit the mass-to-light ratio, and that many

values of the mass-to-light ratio can result in similar maximum likelihoods. This could also be a contributing factor to the differences in the best fit mass-to-light ratios obtained. Most importantly, we find that cored profiles (Burkert, DC14, and Einasto) better fit, in general, the SPARC catalog galaxies, while the Einasto profile tends to have the best fit values for the reduced chi-square.

Finally, we discuss the reproduction of the results from [9], in which, among others, the NFW and Einasto profile

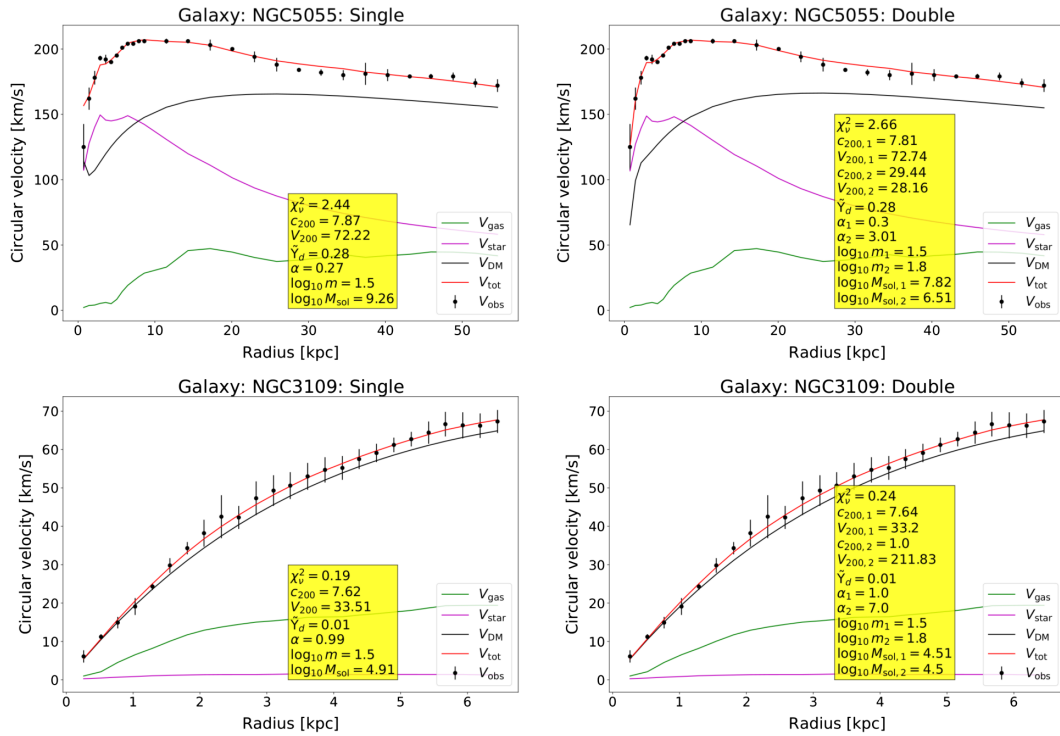


FIG. 11. Particle masses fixed ($m_1 = 10^{1.5} m_{22}$, $m_2 = 10^{1.8} m_{22}$). Rotation curves for galaxies NGC5055 (top row) and NGC3109 (bottom row) for the assumed models: single, summed (left); double, summed (right).

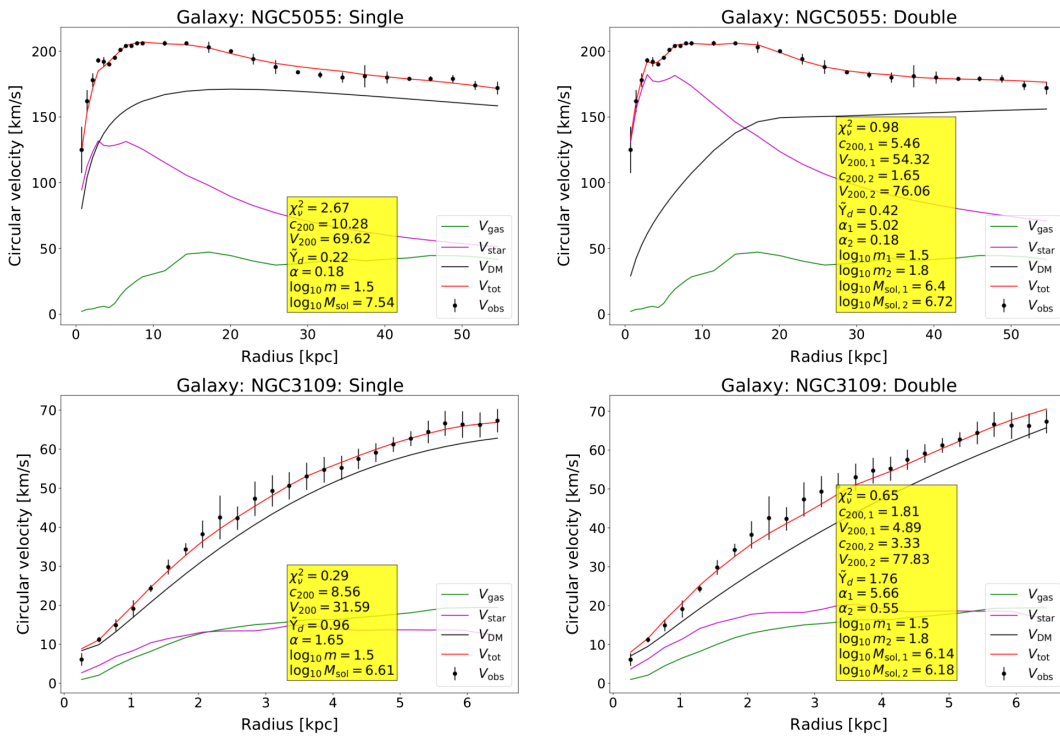


FIG. 12. Particle masses fixed ($m_1 = 10^{1.5} m_{22}$, $m_2 = 10^{1.8} m_{22}$). Rotation curves for galaxies NGC5055 (top row) and NGC3109 (bottom row) for the assumed models: single, matched (left); double, matched (right).

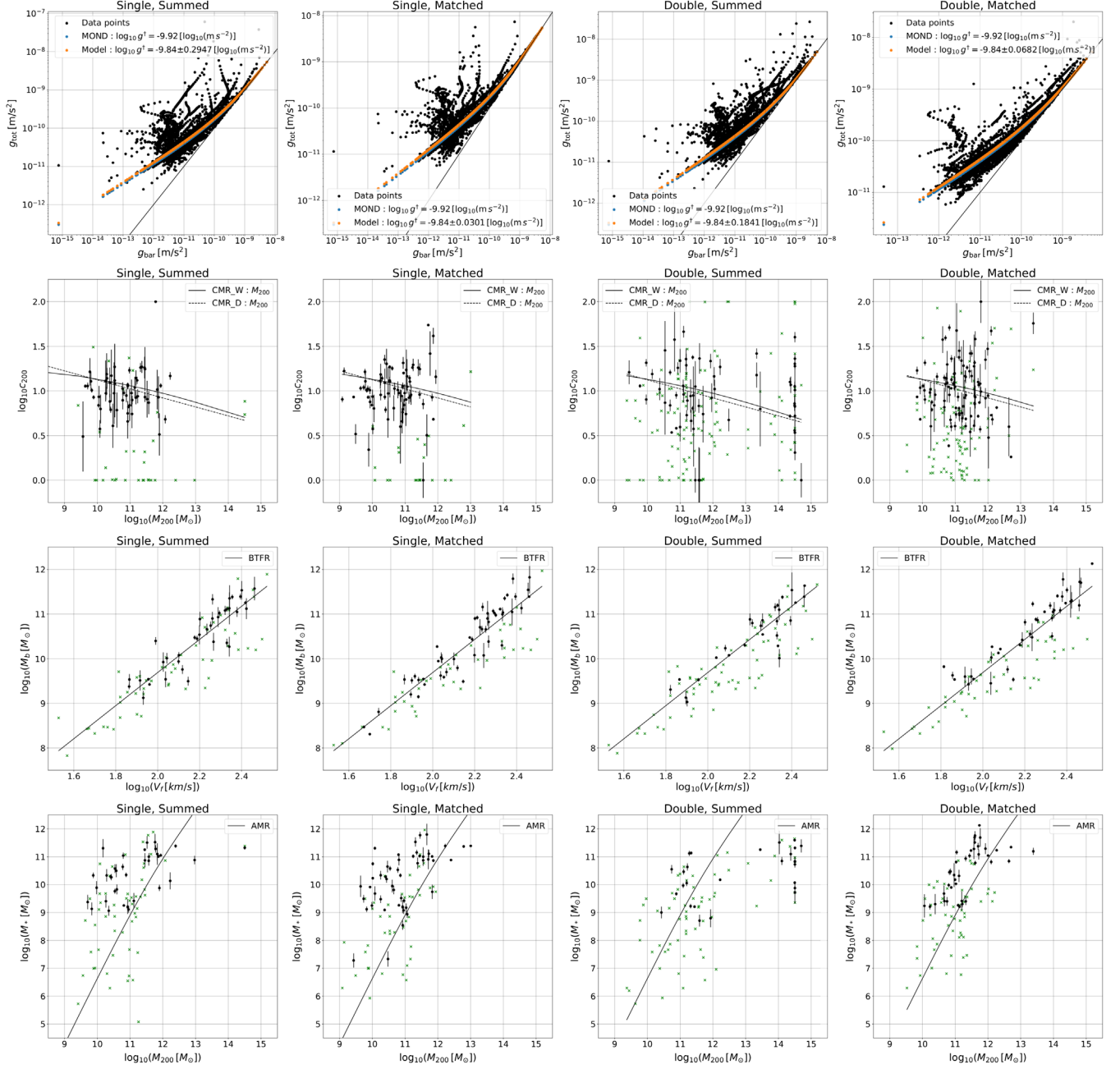


FIG. 13. Particle masses fixed ($m_1 = 10^{1.5}m_{22}$, $m_2 = 10^{1.8}m_{22}$). Empirical relations for the single, summed (left column), single, matched (second column from the left), double, summed (third column from the left), and double, matched (right column) models. Top row: gravitational RARs. Blue points correspond to Eq. (A1) for the MOND value $g_{\ddagger} = 1.2 \times 10^{-10}$ m/s², and orange points to Eq. (A1) with the best fit g_{\ddagger} . Second row from the top: $\log_{10} c_{200}$ vs $\log_{10} M_{200}$. Black solid lines correspond to values calculated from Eq. (A3) and black dashed lines to values calculated from Eq. (A2). Third row from the top: $\log_{10} M_{\text{baryons}}$ (i.e., $M_* + M_{\text{gas}}$) vs $\log_{10} V_f$. Black solid lines correspond to values calculated from Eq. (A4). Bottom row: $\log_{10} M_*$ vs $\log_{10} M_{200}$. Black solid lines correspond to values calculated from Eq. (A5). For the second from the top, third from the top and bottom rows, the points are marked the same as in Fig. 3.

fits for the SPARC galaxies are compared. Here, we take only galaxies with a total number of measured circular velocities $N \geq 10$ and a quality flag less than three, leaving a total of 121 galaxies analyzed as in [9]. We take uniform priors and

constrain the ranges of parameters to be $1 \leq c_{200} \leq 100$, $1 \leq V_{200} \leq 500$, $0.01 \leq \tilde{\Upsilon}_d \leq 5$, and $10^{-3} \leq \alpha \leq 10$. We also take $\tilde{\Upsilon}_b = 1.4\tilde{\Upsilon}_d$ and minimize the chi-squared given by

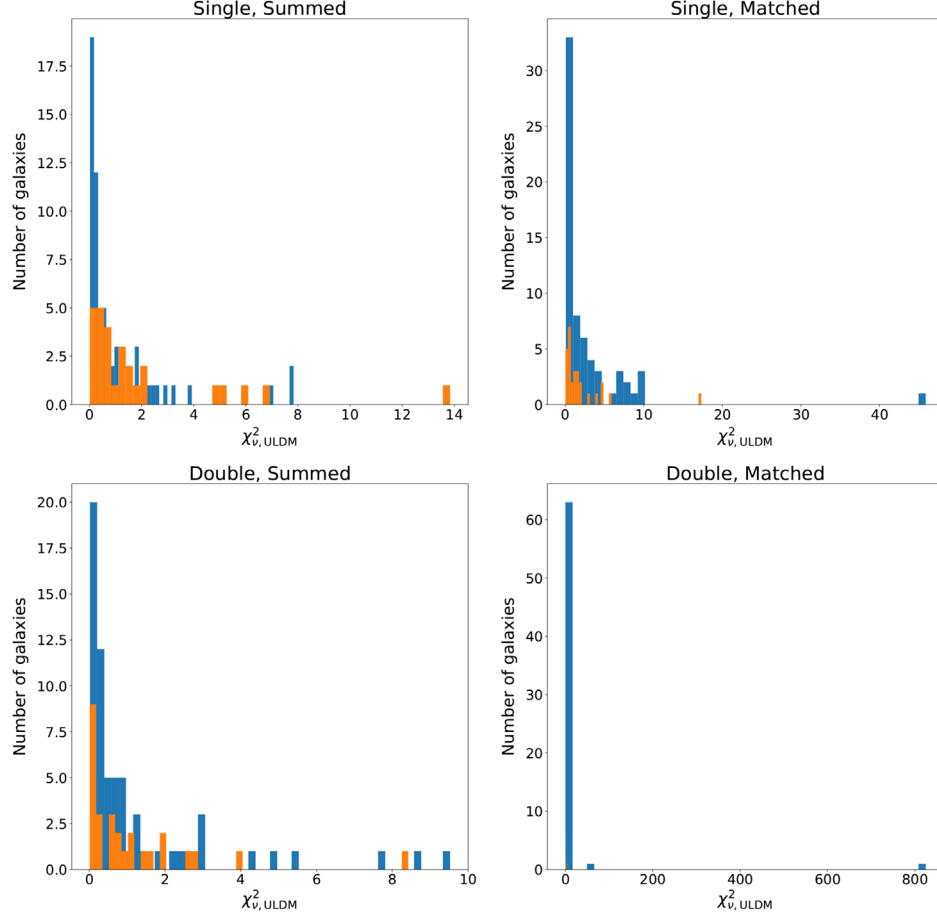


FIG. 14. Particle mass free. Reduced chi-square χ_v^2 for the assumed models: single, summed (top, left); single, matched (top, right); double, summed (bottom, left); double, matched (bottom, right).

$$\chi_{\Upsilon}^2 = \left(\frac{\tilde{\Upsilon}_d - \tilde{\Upsilon}_d}{\sigma_{\Upsilon_d}} \right)^2 + \chi^2, \quad (\text{B1})$$

where χ^2 is given by Eq. (3.4).

With this analysis, we confirm that the Einasto profile gives a reduced chi-square closer to one than the NFW profile for many of the galaxies analyzed. We are able to approximately reproduce Figs. 1, 6, and 11 (for the Einasto and NFW profiles) of [9]. We find the mean and median reduced chi-squared for all galaxies analyzed to be $\chi_{\nu, \text{NFW}}^{2, \text{median}} = 1.44$, $\chi_{\nu, \text{NFW}}^{2, \text{mean}} = 3.14$, $\chi_{\nu, \text{Einasto}}^{2, \text{median}} = 0.78$, and $\chi_{\nu, \text{Einasto}}^{2, \text{mean}} = 1.69$.

b. Main CDM results

We begin with comparing the use of different priors for each of the CDM models. We perform maximum likelihood estimates for 120 galaxies in the SPARC catalog with inclinations greater than 30° , quality flags not equal to three, and nonzero SPARC measurements for the maximum circular velocity V_f . These galaxies also have a total number of circular velocity measurements greater than four (for galaxies without bulge components) or greater

than five (for galaxies with bulge components), which is the total number of parameters for the Einasto model. The fits are performed for five different cases: (1) uniform priors on all parameters with the possible parameter ranges discussed previously; (2) case (1) with the change $0 < c_{200} < \infty$; (3) case (1) with the change $0 < V_{200} < \infty$; (4) case (1) with the change $0 < \tilde{\Upsilon}_d < \infty$; (5) case (1) with the change $0 < \tilde{\Upsilon}_b < \infty$.

Figure 19 shows the distributions of the difference in the BIC statistics for each of the SPARC galaxies analyzed. Each of the prior cases (2)–(5) are compared to prior case (1) with the definition $\Delta \text{BIC} = \text{BIC}_{(1)} - \text{BIC}_{(i)}$, where $i = 2$ corresponds to the top row, $i = 3$ to the second row from the top, $i = 4$ to the third row from the top, and $i = 5$ to the bottom row. The Burkert model corresponds to the left column, the DC14 model to the second column from the left, the Einasto model to the third column from the left, and the NFW model to the right column.

The DC14 model should be viewed differently from the other models for this particular test of different prior cases. This is due to the fact that one of the parameters in the DC14 model, V_{200} , is constrained from $\log_{10}(M_*/M_{\text{halo}}) < -1.3$.

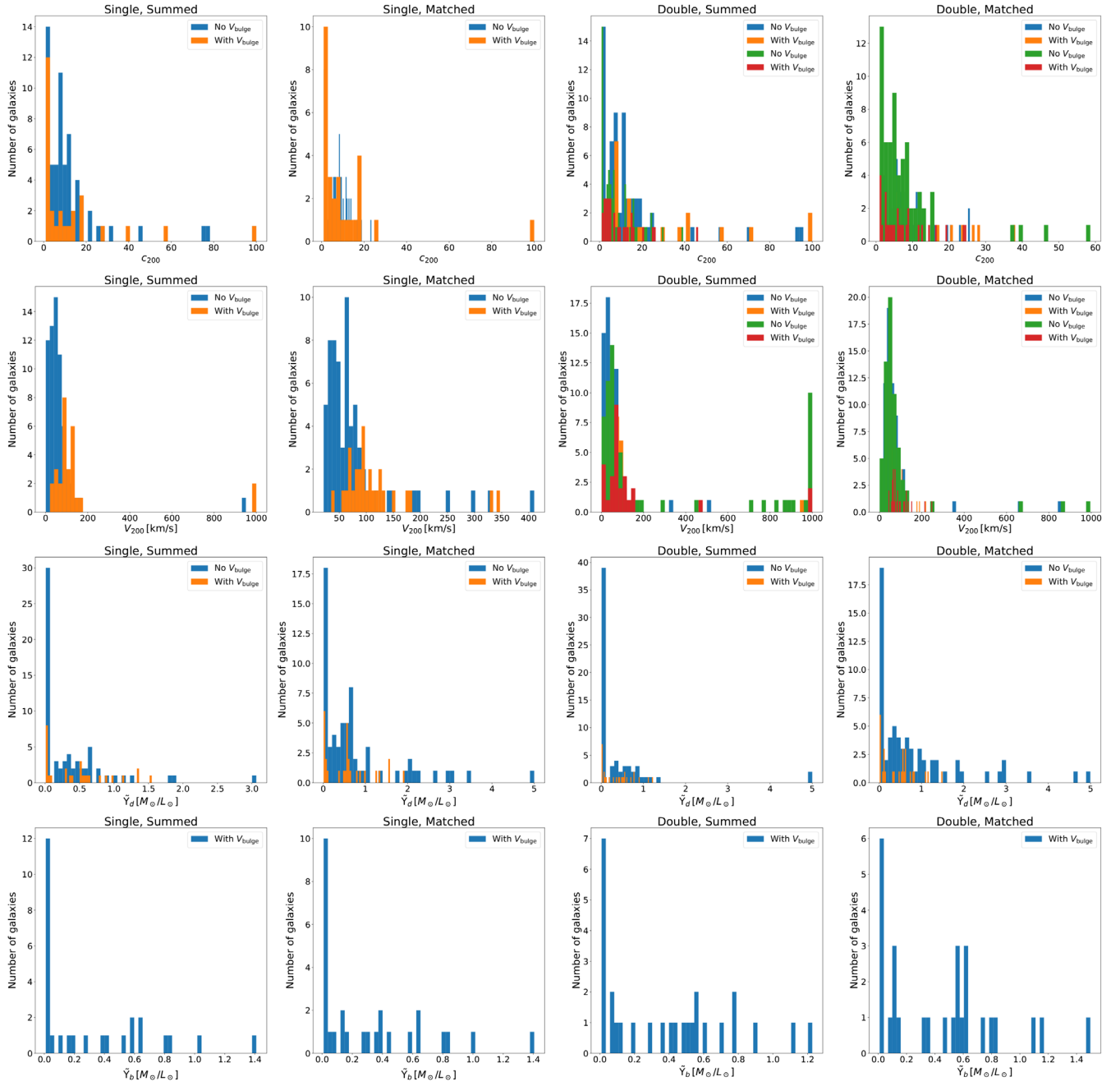


FIG. 15. Particle mass free. Distributions for c_{200} (top row), V_{200} (second from top row), \tilde{Y}_d (third from top row), and \tilde{Y}_b (bottom row) for the single flavor summed (left column), single flavor matched (second column from the left), double flavor summed (third column from the left), and double flavor matched (right column) models.

Therefore, for prior case (2), c_{200} is constrained to a finite parameter range due to the constraint on V_{200} , and vice versa for prior case (3). Nonetheless, the DC14 model seems to have the strongest dependence on the parameter ranges chosen for c_{200} and \tilde{Y}_d compared to the other models, while there are some outliers for the other models.

Now, we discuss how the different CDM models compare to each other assuming uniform priors and finite ranges for each free parameter. See Table II for parameter

ranges. Figure 20 shows the BIC for each model compared to the BIC for each other model. The Burkert model is compared to the DC14 model (top left), the Einasto model (top middle), and the NFW model (top right), the DC14 model is compared to the Einasto model (bottom left) and to the NFW model (bottom middle). Finally, the Einasto model is compared to the NFW model (bottom right). The lines for $\Delta\text{BIC} = 0$, $|\Delta\text{BIC}| = 2$, $|\Delta\text{BIC}| = 6$, and $|\Delta\text{BIC}| = 10$ are displayed as the black dashed, blue, red,

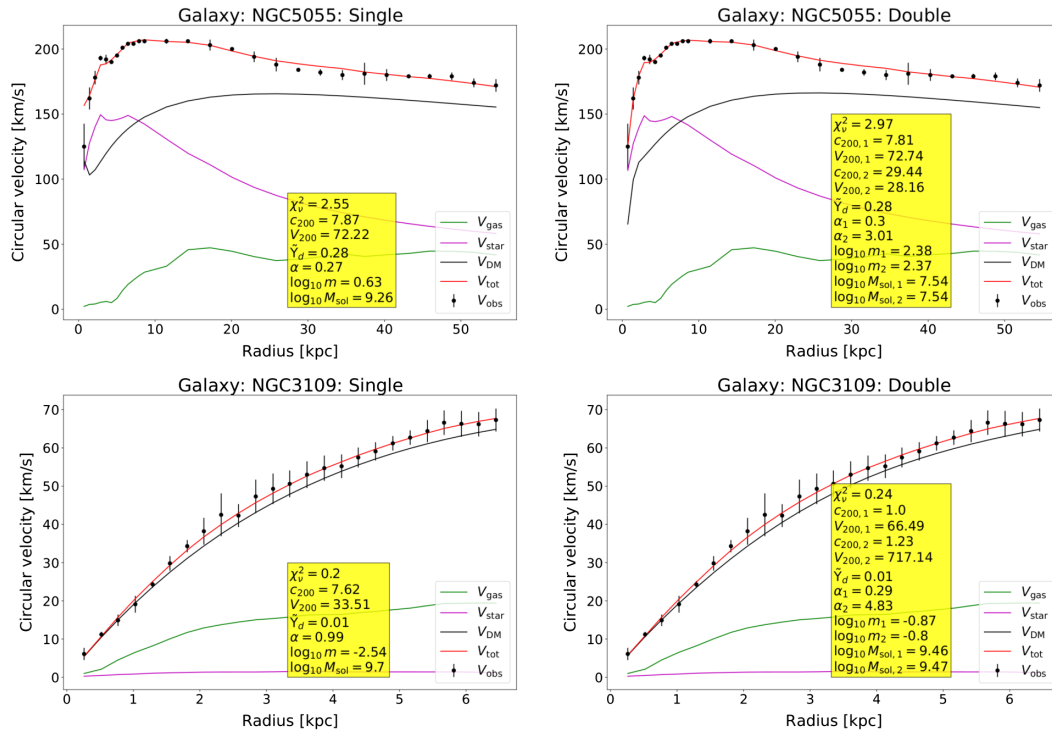


FIG. 16. Particle mass free. Rotation curves for galaxies NGC5055 (top row) and NGC3109 (bottom row) for the assumed models: single, summed (left); double, summed (right).

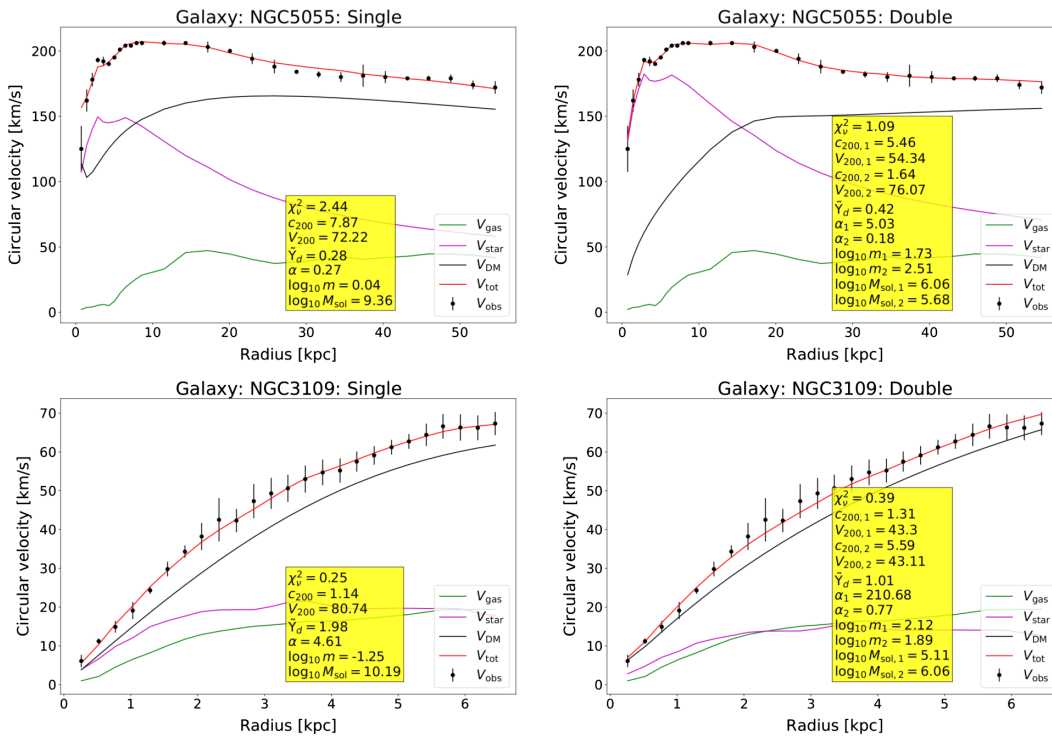


FIG. 17. Particle mass free. Rotation curves for galaxies NGC5055 (top row) and NGC3109 (bottom row) for the assumed models: single, matched (left); double, matched (right).

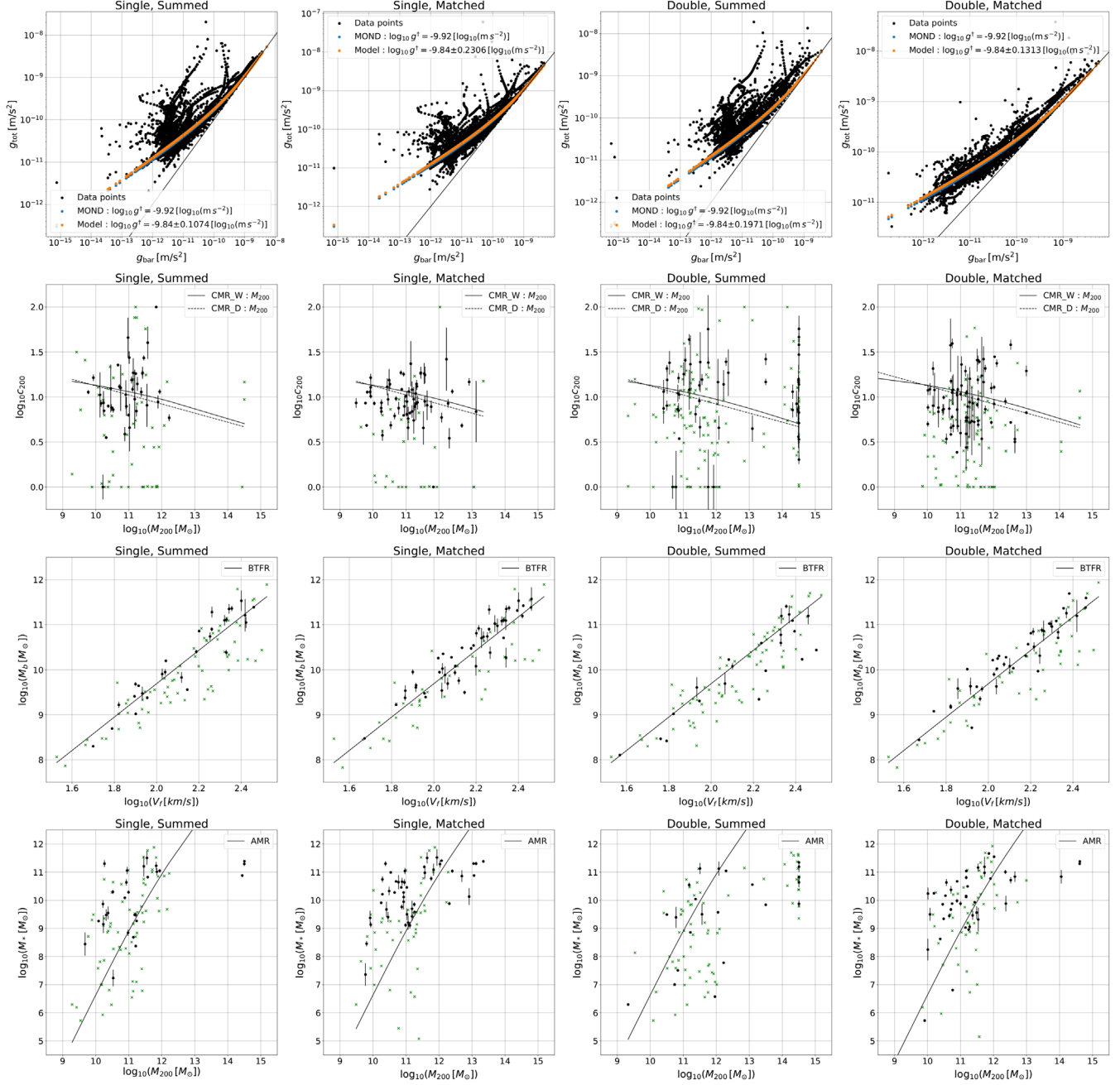


FIG. 18. Particle mass free. Empirical relations for the single, summed (left column), single, matched (second column from the left), double, summed (third column from the left), and double, matched (right column) models. Top row: gravitational RARs. Blue points correspond to Eq. (A1) for the MOND value $g_{\ddagger} = 1.2 \times 10^{-10} \text{ m/s}^2$, and orange points to Eq. (A1) with the best fit g_{\ddagger} . Second row from the top: $\log_{10} c_{200}$ vs $\log_{10} M_{200}$. Black solid lines correspond to values calculated from Eq. (A3) and black dashed lines to values calculated from Eq. (A2). Third row from the top: $\log_{10} M_{\text{baryons}}$ (i.e., $M_{*} + M_{\text{gas}}$) vs $\log_{10} V_f$. Black solid lines correspond to values calculated from Eq. (A4). Bottom row: $\log_{10} M_{*}$ vs $\log_{10} M_{200}$. Black solid lines correspond to values calculated from Eq. (A5). For the second from the top, third from the top and bottom rows, the points are marked the same as in Fig. 3.

and green lines. The fraction of galaxies that fall within a particular range for ΔBIC is shown in the insets.

Both the Burkert and Einasto models tend to perform better than the DC14 and NFW models. However, almost half of the galaxies analyzed show no preference for the either the Burkert or DC14 models. A significant portion of

galaxies show mild evidence for the Burkert model over the Einasto model, while another significant portion shows decisive evidence for the Einasto model.

Finally, we show the resulting statistical and parameter distributions, example rotation curves, and empirical relations for the CDM models:

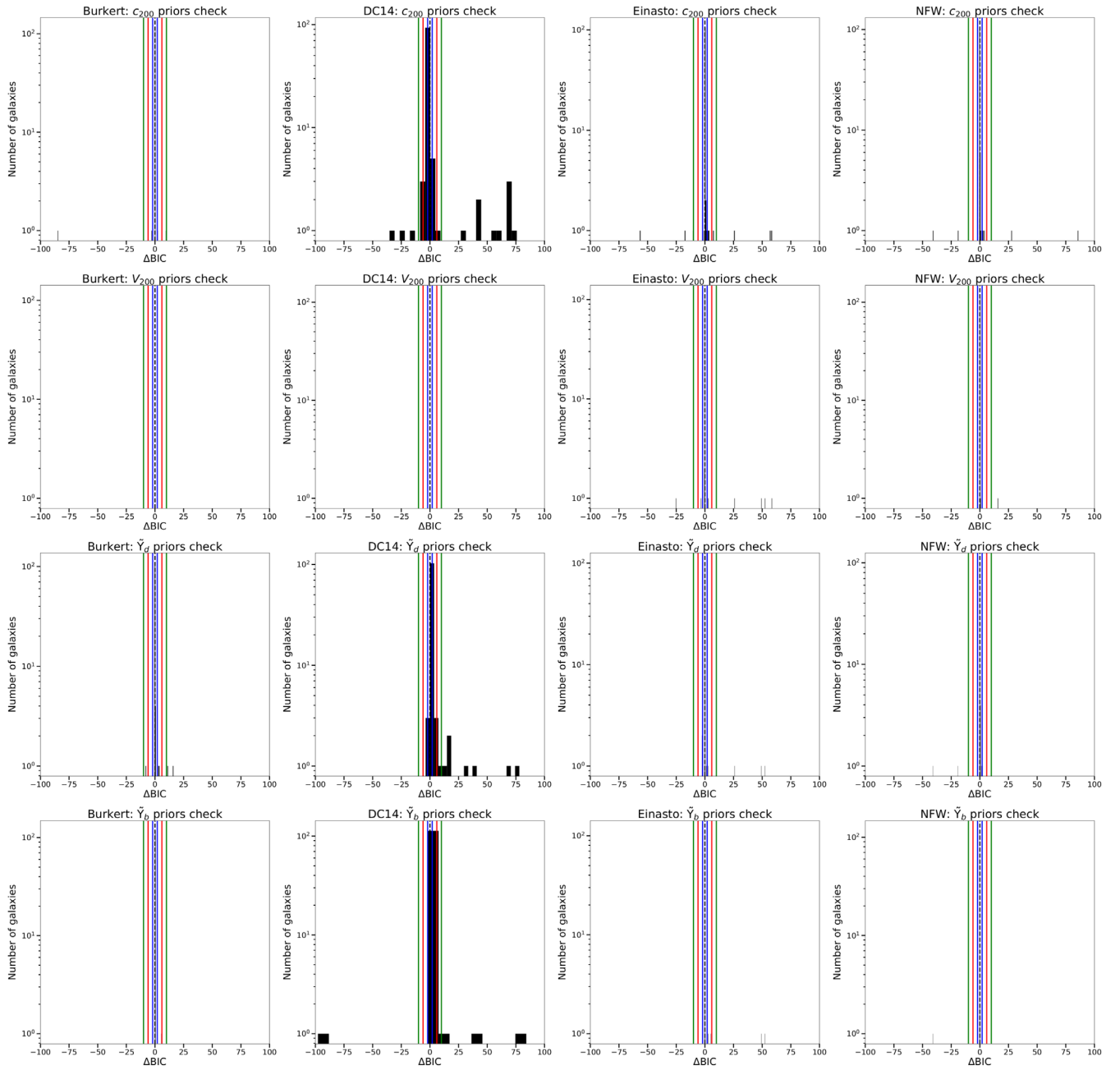


FIG. 19. Distributions of the difference between BIC statistics for different priors cases. We check five different priors cases: (1) uniform priors and finite parameter ranges for all parameters; (2) case (1) with the change $0 < c_{200} < \infty$; (3) case (1) with the change $0 < V_{200} < \infty$; (4) case (1) with the change $0 < \tilde{Y}_d < \infty$; (5) case (1) with the change $0 < \tilde{Y}_b < \infty$. The difference between BIC statistics is given by as $\Delta\text{BIC} = \text{BIC}_{(1)} - \text{BIC}_{(i)}$, where $i = 2$ corresponds to the top row, $i = 3$ to the second row from the top, $i = 4$ to the third row from the top, and $i = 5$ to the bottom row. The Burkert model corresponds to the left column, the DC14 model to the second column from the left, the Einasto model to the third column from the left, and the NFW model to the right column.

- (i) Figure 21 shows the reduced chi-square values.
- (ii) Figure 22 shows the parameter distributions for each of the CDM models. The second from the bottom and bottom rows show the distributions of \tilde{Y}_d and \tilde{Y}_b , respectively. For each model, the \tilde{Y}_d distribution tends to peak near the lower boundary of 0.01, while

for the Einasto and NFW models, the \tilde{Y}_b distribution also tends to peak near the lower boundary of 0.01. For the Burkert, the distribution of \tilde{Y}_b has equal numbers of galaxies showing preference for the lower boundary of 0.01 and ≈ 0.6 . For the DC14, the distribution of \tilde{Y}_b tends to peak around ≈ 0.6 .

TABLE II. Parameter ranges for each of the CDM models tested. For the DC14 model, V_m corresponds to the minimum virial velocity found from $\log_{10}(M_*/M_{\text{halo}}) < -1.3$.

Parameters	Models			
	Burkert	DC14	Einasto	NFW
c_{200}	$[1, 10^2]$	$[1, 10^2]$	$[1, 10^2]$	$[1, 10^2]$
V_{200} [km s $^{-1}$]	$[1, 10^3]$	$[V_m, 10^3]$	$[1, 10^3]$	$[1, 10^3]$
$\tilde{\Upsilon}_d$	$[0.01, 5]$	$[0.01, 5]$	$[0.01, 5]$	$[0.01, 5]$
$\tilde{\Upsilon}_b$	$[0.01, 5]$	$[0.01, 5]$	$[0.01, 5]$	$[0.01, 5]$
α	$(-\infty, \infty)$...

- (iii) Figure 23 shows rotation curves for the galaxies NGC5055 and NGC3109 for each of the CDM models.
- (iv) Figure 24 shows example galaxies for which the degeneracy in the best fit $\tilde{\Upsilon}_d$ is strong or weak.
- (v) Figure 25 shows the empirical relations analyzed (the gravitational RAR of [40], the CMR [11,35], the

BTFR [38], and the AMR [36,37]). As in Figs. 13 and 18, all models give a value of g^\dagger that is close to the MOND value. All models tend to give significant scatter around both CMR relations, around the BTFR relation, and around the AMR relation, with less scatter around the BTFR relation.

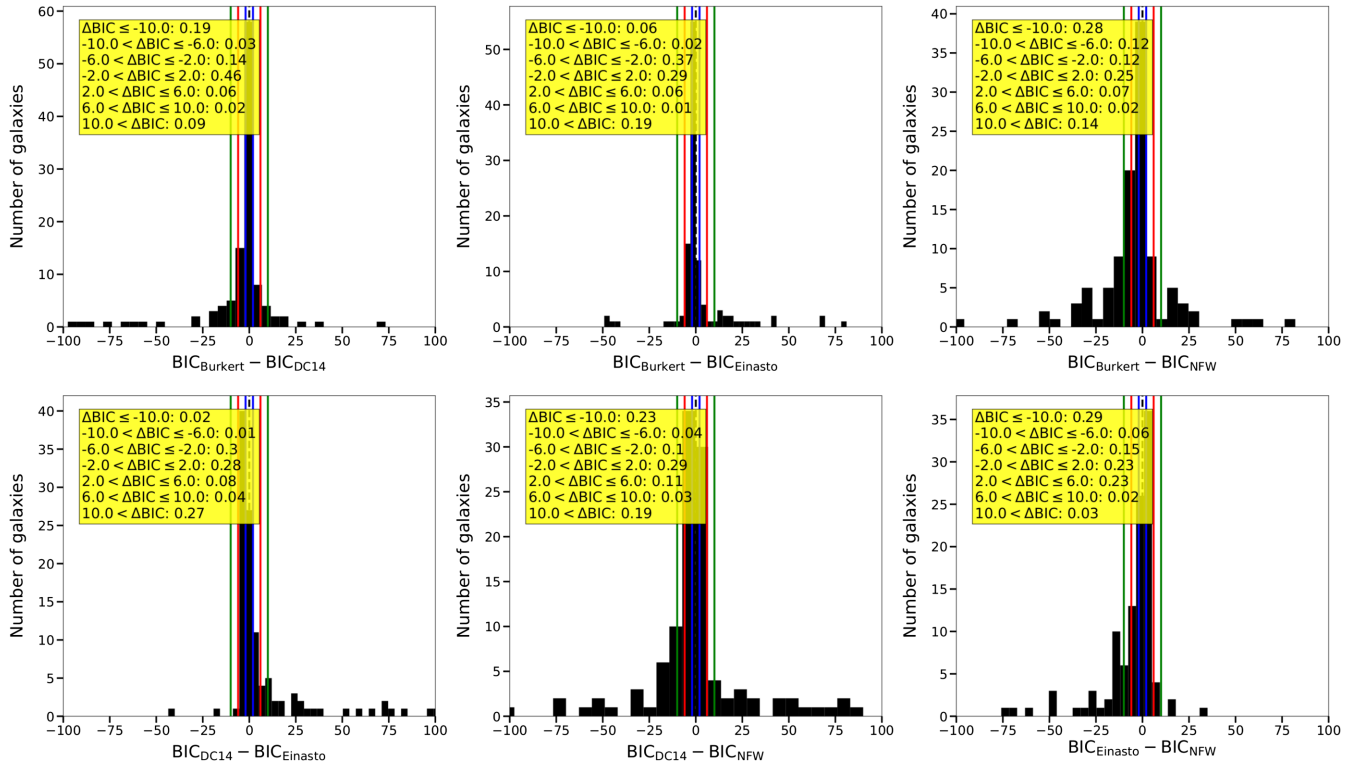


FIG. 20. BIC statistics for Burkert vs DC14 (top left), Burkert vs Einasto (top middle), Burkert vs NFW (top right), DC14 vs Einasto (bottom left), DC14 vs NFW (bottom middle), and Einasto vs NFW (bottom right). Black points correspond to each of the galaxies analyzed, the black dashed line corresponds to $\Delta\text{BIC} = 0$, blue lines correspond to $|\Delta\text{BIC}| = 2$, red lines to $|\Delta\text{BIC}| = 6$, and green lines to $|\Delta\text{BIC}| = 10$. Inset is the fraction of galaxies that fall within a given range for ΔBIC .

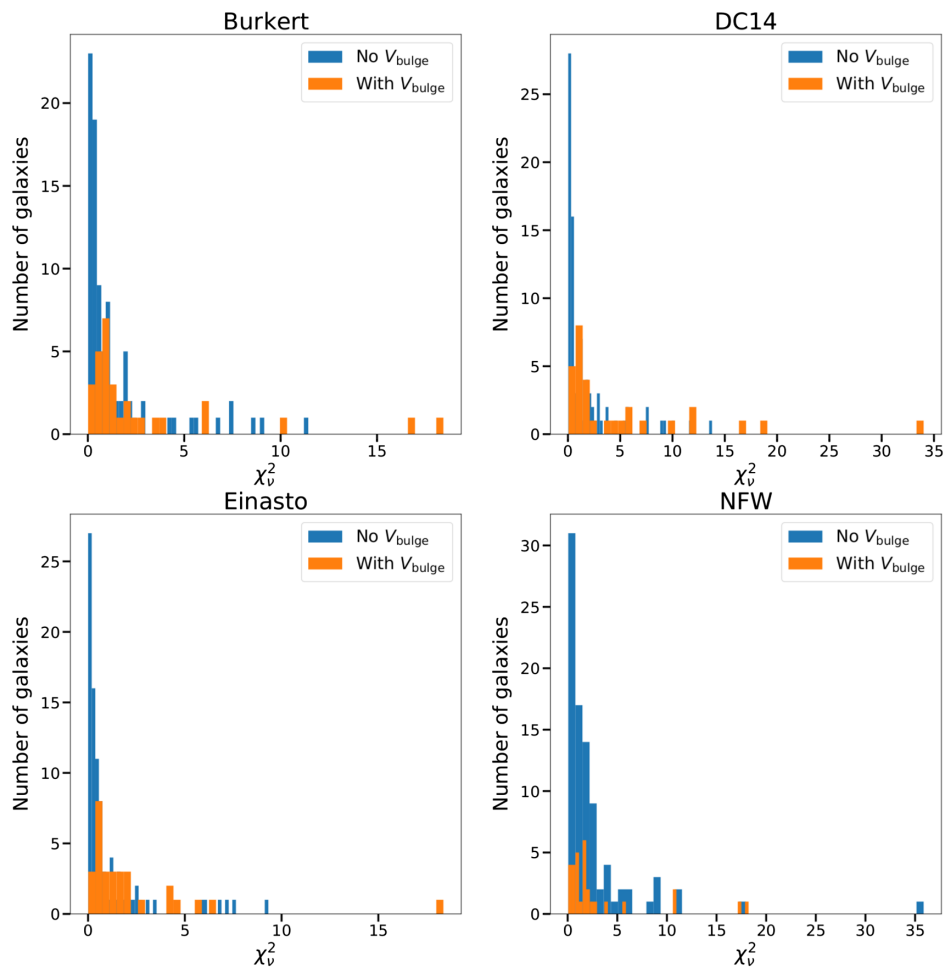


FIG. 21. Reduced chi-square χ^2_ν for the Burkert (top left), DC14 (top right), Einasto (bottom left), and the NFW (bottom right) models.

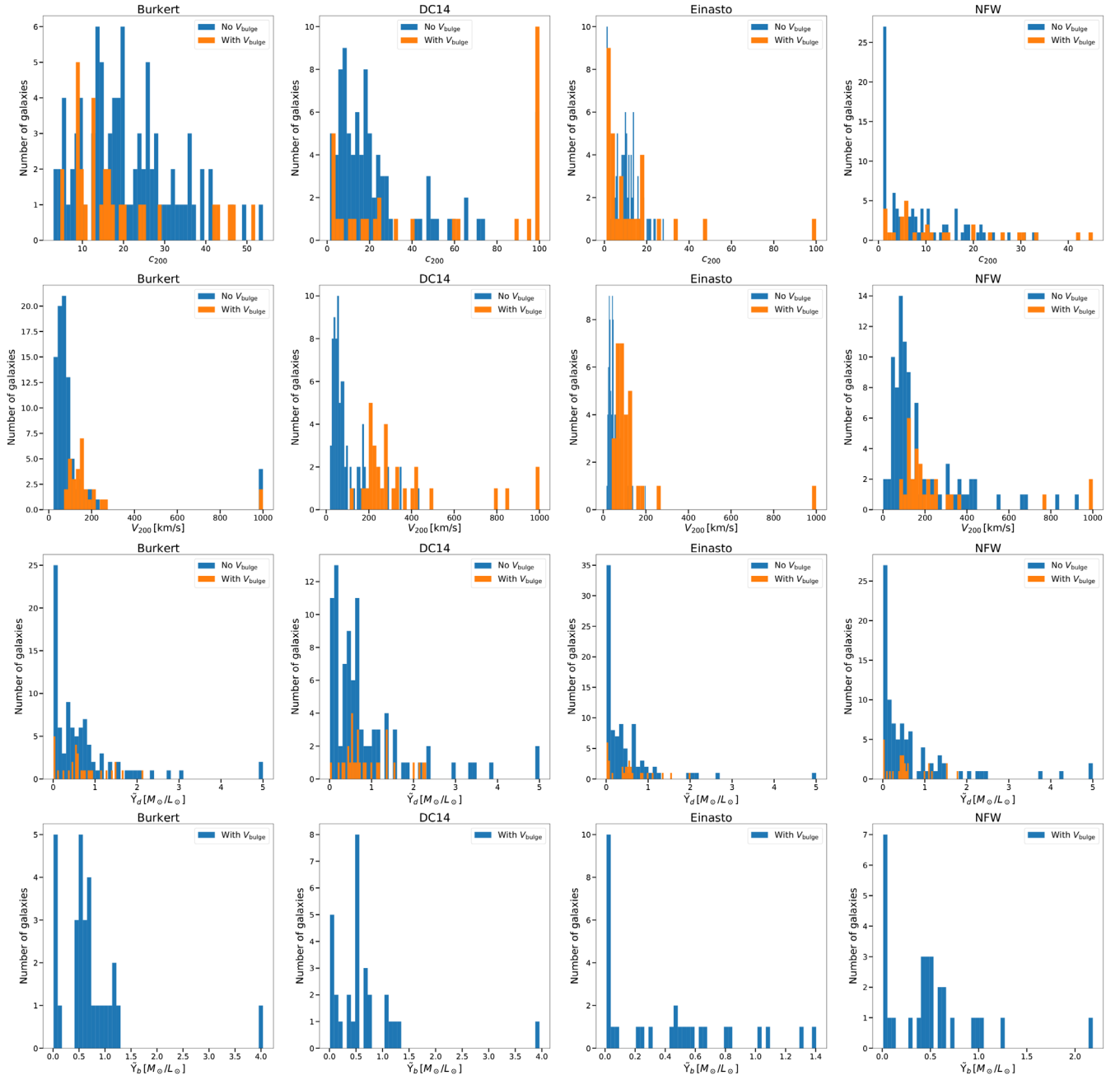


FIG. 22. Distributions for c_{200} (top row), V_{200} (second from top row), \tilde{Y}_d (third from top row), and \tilde{Y}_b (bottom row) for the Burkert (left column), DC14 (second from left column), Einasto (third from left column), and the NFW (right column) models.

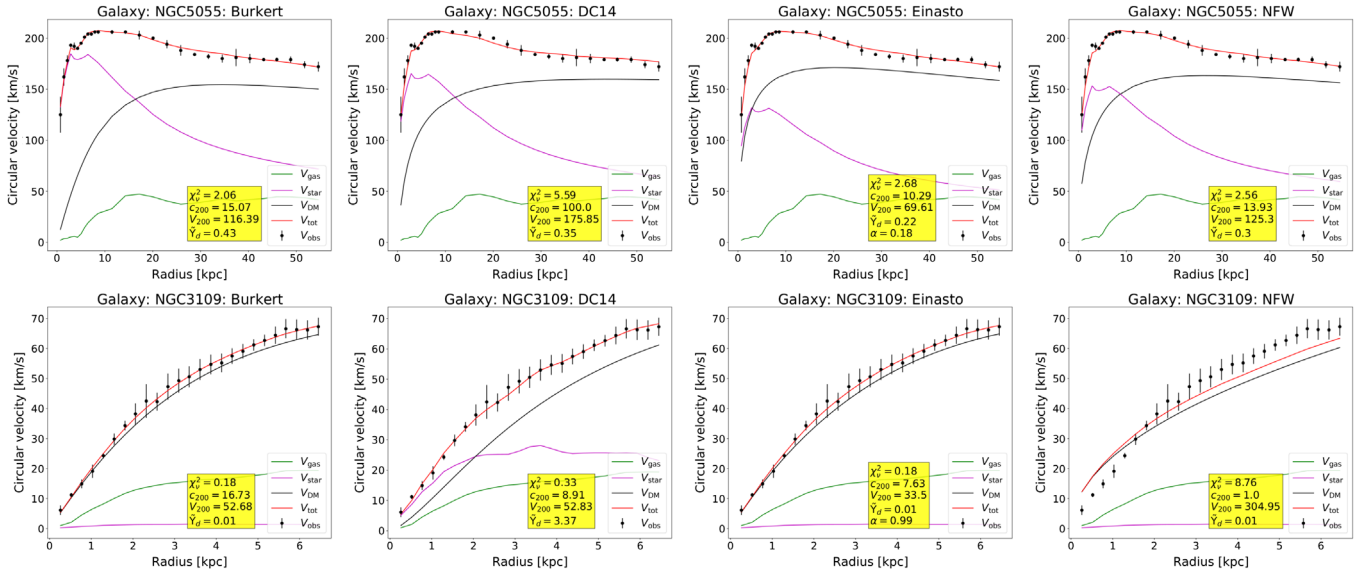


FIG. 23. Rotation curves for galaxies NGC5055 (top row) and NGC3109 (bottom row) for the Burkert (left column), DC14 (second from left column), Einasto (third from left column), and the NFW (right column) models.

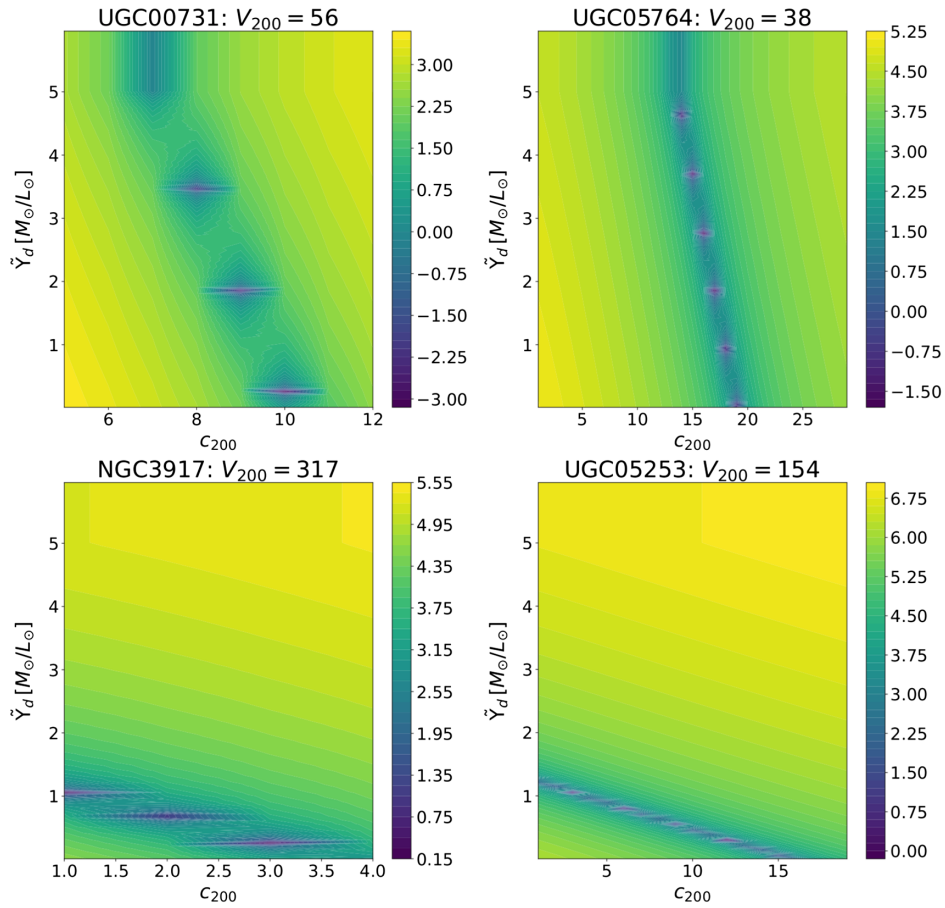


FIG. 24. Galaxies for which the best fit \tilde{Y}_d is strongly degenerate (top row) and those for which the degeneracy is weaker (bottom row).

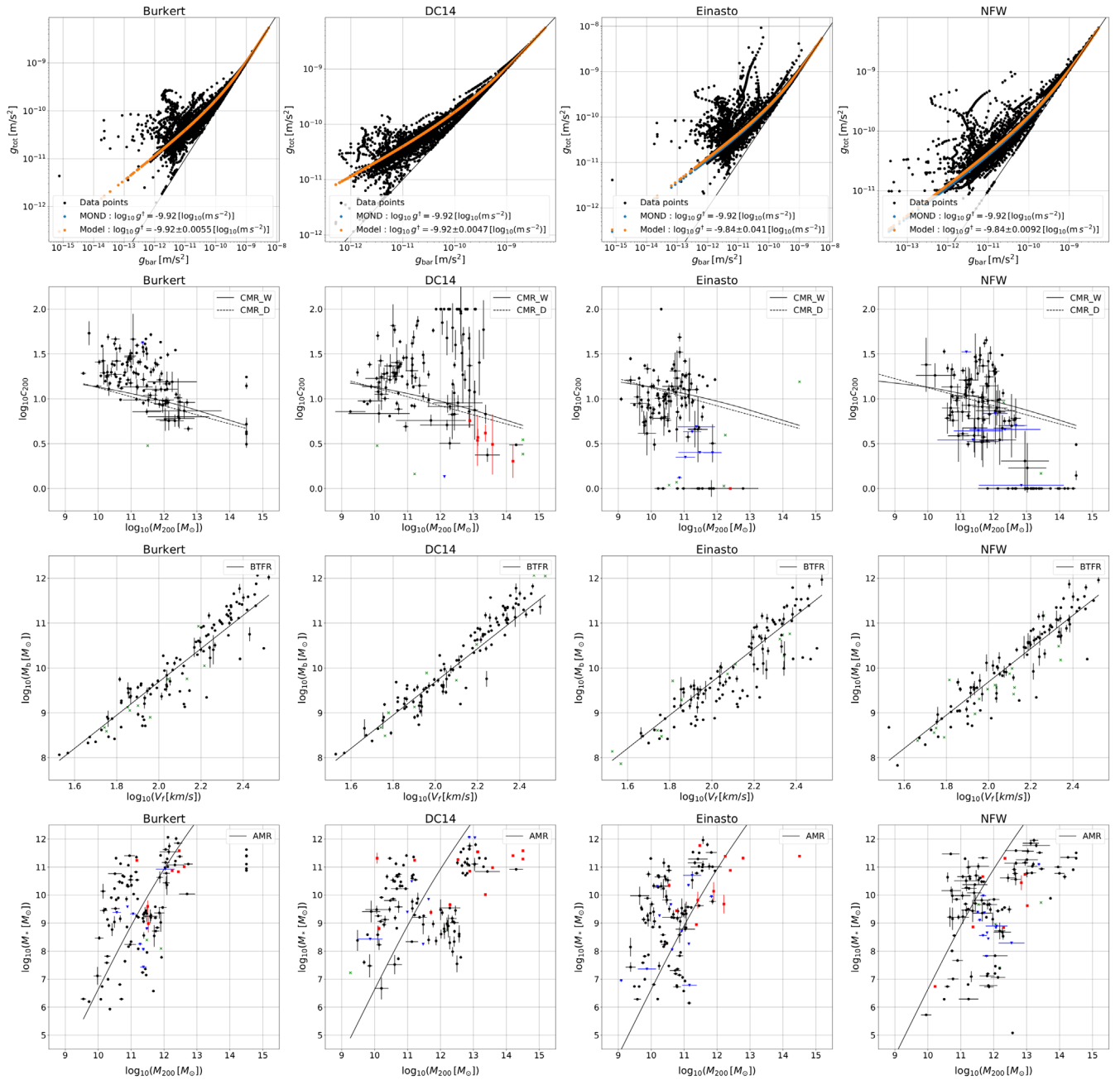


FIG. 25. Empirical relations for the Burkert (left column), DC14 (second column from the left), Einasto (third column from the left), and NFW (right column) models. Top row: gravitational RARs. Blue points correspond to Eq. (A1) for the MOND value $g_{\ddagger} = 1.2 \times 10^{-10} \text{ m/s}^2$, and orange points to Eq. (A1) with the best fit g_{\ddagger} . Second row from the top: $\log_{10} c_{200}$ vs $\log_{10} M_{200}$. Black solid lines correspond to values calculated from Eq. (A3) and black dashed lines to values calculated from Eq. (A2). Third row from the top: $\log_{10} M_{\text{baryons}}$ (i.e., $M_{*} + M_{\text{gas}}$) vs $\log_{10} V_f$. Black solid lines correspond to values calculated from Eq. (A4). Bottom row: $\log_{10} M_{*}$ vs $\log_{10} M_{200}$. Black solid lines correspond to values calculated from Eq. (A5). For the second from the top, third from the top and bottom rows, the points are marked the same as in Fig. 3.

- [1] J. F. Navarro, C. S. Frenk, and S. D. M. White, The structure of cold dark matter halos, *Astrophys. J.* **462**, 563 (1996).
- [2] J. F. Navarro, C. S. Frenk, and S. D. M. White, A universal density profile from hierarchical clustering, *Astrophys. J.* **490**, 493 (1997).
- [3] J. F. Navarro, A. Ludlow, V. Springel, J. Wang, M. Vogelsberger, S. D. M. White, A. Jenkins, C. S. Frenk, and A. Helmi, The diversity and similarity of simulated cold dark matter haloes, *Mon. Not. R. Astron. Soc.* **402**, 21 (2010).
- [4] A. Burkert, The structure of dark matter halos in dwarf galaxies, *Astrophys. J. Lett.* **447**, L25 (1995).
- [5] J. S. Bullock and M. Boylan-Kolchin, Small-scale challenges to the Λ CDM paradigm, *Annu. Rev. Astron. Astrophys.* **55**, 343 (2017).
- [6] A. Del Popolo and M. Le Delliou, Review of solutions to the cusp-core problem of the Λ CDM model, *Galaxies* **9**, 123 (2021).
- [7] L. V. Sales, A. Wetzel, and A. Fattahi, Baryonic solutions and challenges for cosmological models of dwarf galaxies, [arXiv:2206.05295](https://arxiv.org/abs/2206.05295).
- [8] D. C. Rodrigues, A. del Popolo, V. Marra, and P. L. C. de Oliveira, Evidence against cuspy dark matter haloes in large galaxies, *Mon. Not. R. Astron. Soc.* **470**, 2410 (2017).
- [9] N. Loizeau and G. R. Farrar, Galaxy rotation curves disfavor traditional and self-interacting dark matter halos, preferring a disk component or einasto function, *Astrophys. J. Lett.* **920**, L10 (2021).
- [10] F. Lelli, S. S. McGaugh, and J. M. Schombert, SPARC: Mass models for 175 disk galaxies with spitzer photometry and accurate rotation curves, *Astron. J.* **152**, 157 (2016).
- [11] J. Wang, S. Bose, C. S. Frenk, L. Gao, A. Jenkins, V. Springel, and S. D. M. White, Universal structure of dark matter haloes over a mass range of 20 orders of magnitude, *Nature (London)* **585**, 39 (2020).
- [12] S. Mashchenko, H. M. P. Couchman, and J. Wadsley, The removal of cusps from galaxy centres by stellar feedback in the early Universe, *Nature (London)* **442**, 539 (2006).
- [13] S. Mashchenko, J. Wadsley, and H. M. P. Couchman, Stellar feedback in dwarf galaxy formation, *Science* **319**, 174 (2008).
- [14] F. Governato, C. Brook, L. Mayer, A. Brooks, G. Rhee, J. Wadsley *et al.*, Bulgeless dwarf galaxies and dark matter cores from supernova-driven outflows, *Nature (London)* **463**, 203 (2010).
- [15] F. Governato, A. Zolotov, A. Pontzen, C. Christensen, S. H. Oh, A. M. Brooks, T. Quinn, S. Shen, and J. Wadsley, Cuspy no more: How outflows affect the central dark matter and baryon distribution in Λ cold dark matter galaxies, *Mon. Not. R. Astron. Soc.* **422**, 1231 (2012).
- [16] A. D. Popolo, The cusp/core problem and the secondary infall model, *Astrophys. J.* **698**, 2093 (2009).
- [17] A. El-Zant, I. Shlosman, and Y. Hoffman, Dark halos: The flattening of the density cusp by dynamical friction, *Astrophys. J.* **560**, 636 (2001).
- [18] A. A. El-Zant, Y. Hoffman, J. Primack, F. Combes, and I. Shlosman, Flat-cored dark matter in cuspy clusters of galaxies, *Astrophys. J.* **607**, L75 (2004).
- [19] S.-H. Oh, C. Brook, F. Governato, E. Brinks, L. Mayer, W. J. G. de Blok *et al.*, The central slope of dark matter cores in dwarf galaxies: Simulations versus things, *Astrophys. J.* **142**, 24 (2011).
- [20] A. Di Cintio, C. B. Brook, A. V. Macciò, G. S. Stinson, A. Knebe, A. A. Dutton, and J. Wadsley, The dependence of dark matter profiles on the stellar-to-halo mass ratio: A prediction for cusps versus cores, *Mon. Not. R. Astron. Soc.* **437**, 415 (2014).
- [21] A. D. Cintio, C. B. Brook, A. A. Dutton, A. V. Macciò, G. S. Stinson, and A. Knebe, A mass-dependent density profile for dark matter haloes including the influence of galaxy formation, *Mon. Not. R. Astron. Soc.* **441**, 2986 (2014).
- [22] C. B. Brook, The variation of rotation curve shapes as a signature of the effects of baryons on dark matter density profiles, *Mon. Not. R. Astron. Soc.* **454**, 1719 (2015).
- [23] C. B. Brook and A. Di Cintio, Signatures of dark matter halo expansion in galaxy populations, *Mon. Not. R. Astron. Soc.* **453**, 2133 (2015).
- [24] H. Katz, F. Lelli, S. S. McGaugh, A. Di Cintio, C. B. Brook, and J. M. Schombert, Testing feedback-modified dark matter haloes with galaxy rotation curves: Estimation of halo parameters and consistency with Λ CDM scaling relations, *Mon. Not. R. Astron. Soc.* **466**, 1648 (2017).
- [25] T. K. Chan, D. Kereš, J. Oñorbe, P. F. Hopkins, A. L. Muratov, C. A. Faucher-Giguère, and E. Quataert, The impact of baryonic physics on the structure of dark matter haloes: The view from the FIRE cosmological simulations, *Mon. Not. R. Astron. Soc.* **454**, 2981 (2015).
- [26] P. Li, F. Lelli, S. McGaugh, and J. Schombert, A comprehensive catalog of dark matter halo models for SPARC galaxies, *Astrophys. J. Suppl. Ser.* **247**, 31 (2020).
- [27] J. Freundlich, F. Jiang, A. Dekel, N. Cornuault, O. Ginzburg, R. Koskas, S. Lapiner, A. Dutton, and A. V. Macciò, The Dekel-Zhao profile: A mass-dependent dark-matter density profile with flexible inner slope and analytic potential, velocity dispersion, and lensing properties, *Mon. Not. R. Astron. Soc.* **499**, 2912 (2020).
- [28] A. Lazar, J. S. Bullock, M. Boylan-Kolchin, T. K. Chan, P. F. Hopkins, A. S. Graus *et al.*, A dark matter profile to model diverse feedback-induced core sizes of Λ CDM haloes, *Mon. Not. R. Astron. Soc.* **497**, 2393 (2020).
- [29] J. S. Bullock and M. Boylan-Kolchin, Small-scale challenges to the Λ CDM paradigm, *Annu. Rev. Astron. Astrophys.* **55**, 343 (2017).
- [30] M. Milgrom, A modification of the Newtonian dynamics as a possible alternative to the hidden mass hypothesis, *Astrophys. J.* **270**, 365 (1983).
- [31] M. Milgrom, A modification of the Newtonian dynamics—Implications for galaxies, *Astrophys. J.* **270**, 371 (1983).
- [32] A. Kamada, M. Kaplinghat, A. B. Pace, and H.-B. Yu, How the Self-Interacting Dark Matter Model Explains the Diverse Galactic Rotation Curves, *Phys. Rev. Lett.* **119**, 111102 (2017).
- [33] T. Ren, A. Kwa, M. Kaplinghat, and H.-B. Yu, Reconciling the Diversity and Uniformity of Galactic Rotation Curves with Self-Interacting Dark Matter, *Phys. Rev. X* **9**, 031020 (2019).

- [34] F. Kahlhoefer, M. Kaplinghat, T.R. Slatyer, and C.-L. Wu, Diversity in density profiles of self-interacting dark matter satellite halos, *J. Cosmol. Astropart. Phys.* **12** (2019) 010.
- [35] A. A. Dutton and A. V. Macciò, Cold dark matter haloes in the Planck era: Evolution of structural parameters for Einasto and NFW profiles, *Mon. Not. R. Astron. Soc.* **441**, 3359 (2014).
- [36] P. S. Behroozi, R. H. Wechsler, and C. Conroy, The average star formation histories of galaxies in dark matter halos from $z = 0 - 8$, *Astrophys. J.* **770**, 57 (2013).
- [37] P. S. Behroozi, R. H. Wechsler, and C. Conroy, On the lack of evolution in galaxy star formation efficiency, *Astrophys. J.* **762**, L31 (2013).
- [38] F. Lelli, S. S. McGaugh, and J. M. Schombert, The small scatter of the baryonic tully-fisher relation, *Astrophys. J.* **816**, L14 (2015).
- [39] J. M. Schombert and S. McGaugh, Stellar populations and the star formation histories of LSB galaxies: IV spitzer surface photometry of LSB galaxies, *Pub. Astron. Soc. Aust.* **31**, e011 (2014).
- [40] S. S. McGaugh, F. Lelli, and J. M. Schombert, Radial Acceleration Relation in Rotationally Supported Galaxies, *Phys. Rev. Lett.* **117**, 201101 (2016).
- [41] R. D. Peccei and H. R. Quinn, CP Conservation in the Presence of Instantons, *Phys. Rev. Lett.* **38**, 1440 (1977).
- [42] S. Weinberg, A New Light Boson?, *Phys. Rev. Lett.* **40**, 223 (1978).
- [43] F. Wilczek, Problem of Strong P and T Invariance in the Presence of Instantons, *Phys. Rev. Lett.* **40**, 279 (1978).
- [44] A. Arvanitaki, S. Dimopoulos, S. Dubovsky, N. Kaloper, and J. March-Russell, String axiverse, *Phys. Rev. D* **81**, 123530 (2010).
- [45] D. E. Kaplan and R. Rattazzi, Large field excursions and approximate discrete symmetries from a clockwork axion, *Phys. Rev. D* **93**, 085007 (2016).
- [46] D. J. Kaup, Klein-Gordon geon, *Phys. Rev.* **172**, 1331 (1968).
- [47] R. Ruffini and S. Bonazzola, Systems of selfgravitating particles in general relativity and the concept of an equation of state, *Phys. Rev.* **187**, 1767 (1969).
- [48] J. Breit, S. Gupta, and A. Zaks, Cold bose stars, *Phys. Lett. B* **140**, 329 (1984).
- [49] M. Colpi, S. L. Shapiro, and I. Wasserman, Boson Stars: Gravitational Equilibria of Selfinteracting Scalar Fields, *Phys. Rev. Lett.* **57**, 2485 (1986).
- [50] E. Seidel and W.-M. Suen, Dynamical evolution of boson stars. 1. Perturbing the ground state, *Phys. Rev. D* **42**, 384 (1990).
- [51] R. Friedberg, T. D. Lee, and Y. Pang, Scalar soliton stars and black holes, *Phys. Rev. D* **35**, 3658 (1987).
- [52] E. Seidel and W. M. Suen, Oscillating Soliton Stars, *Phys. Rev. Lett.* **66**, 1659 (1991).
- [53] T. Lee and Y. Pang, Nontopological solitons, *Phys. Rep.* **221**, 251 (1992).
- [54] T. Matos and L. Arturo Ureña-López, Further analysis of a cosmological model with quintessence and scalar dark matter, *Phys. Rev. D* **63**, 063506 (2001).
- [55] P.-H. Chavanis, Mass-radius relation of Newtonian self-gravitating Bose-Einstein condensates with short-range interactions: I. Analytical results, *Phys. Rev. D* **84**, 043531 (2011).
- [56] P. H. Chavanis and L. Delfini, Mass-radius relation of Newtonian self-gravitating Bose-Einstein condensates with short-range interactions: II. Numerical results, *Phys. Rev. D* **84**, 043532 (2011).
- [57] A. Suárez, V. H. Robles, and T. Matos, A review on the scalar field/bose-einstein condensate dark matter model, in *Accelerated Cosmic Expansion*, edited by C. Moreno González, J. E. Madriz Aguilar, and L. M. Reyes Barrera (Springer International Publishing, Cham, 2014), pp. 107–142.
- [58] J. Eby, P. Suranyi, and L. C. R. Wijewardhana, The lifetime of axion stars, *Mod. Phys. Lett. A* **31**, 1650090 (2016).
- [59] J. Eby, M. Leembruggen, P. Suranyi, and L. C. R. Wijewardhana, Collapse of axion stars, *J. High Energy Phys.* **12** (2016) 066.
- [60] J. Eby, M. Ma, P. Suranyi, and L. C. R. Wijewardhana, Decay of ultralight axion condensates, *J. High Energy Phys.* **01** (2018) 066.
- [61] L. Visinelli, S. Baum, J. Redondo, K. Freese, and F. Wilczek, Dilute and dense axion stars, *Phys. Lett. B* **777**, 64 (2018).
- [62] D. G. Levkov, A. G. Panin, and I. I. Tkachev, Gravitational Bose-Einstein Condensation in the Kinetic Regime, *Phys. Rev. Lett.* **121**, 151301 (2018).
- [63] J. Eby, M. Leembruggen, L. Street, P. Suranyi, and L. Wijewardhana, Approximation methods in the study of boson stars, *Phys. Rev. D* **98**, 123013 (2018).
- [64] E. Braaten and H. Zhang, Colloquium: The physics of axion stars, *Rev. Mod. Phys.* **91**, 041002 (2019).
- [65] C. Kouvaris, E. Papantonopoulos, L. Street, and L. Wijewardhana, Probing bosonic stars with atomic clocks, *Phys. Rev. D* **102**, 063014 (2020).
- [66] H. Zhang, Axion stars, *Symmetry* **12**, 25 (2020).
- [67] J. Eby, M. Leembruggen, L. Street, P. Suranyi, and L. C. R. Wijewardhana, Global view of QCD axion stars, *Phys. Rev. D* **100**, 063002 (2019).
- [68] B. Eggemeier and J. C. Niemeyer, Formation and mass growth of axion stars in axion miniclusters, *Phys. Rev. D* **100**, 063528 (2019).
- [69] K. Kirkpatrick, A. E. Mirasola, and C. Prescod-Weinstein, Relaxation times for Bose-Einstein condensation in axion miniclusters, *Phys. Rev. D* **102**, 103012 (2020).
- [70] J. Eby, L. Street, P. Suranyi, and L. C. R. Wijewardhana, Global view of axion stars with nearly Planck-scale decay constants, *Phys. Rev. D* **103**, 063043 (2021).
- [71] C. Kouvaris, E. Papantonopoulos, L. Street, and L. C. R. Wijewardhana, Using atomic clocks to detect local dark matter halos, *Phys. Rev. D* **104**, 103025 (2021).
- [72] M. S. Turner, Coherent scalar-field oscillations in an expanding Universe, *Phys. Rev. D* **28**, 1243 (1983).
- [73] W. H. Press, B. S. Ryden, and D. N. Spergel, Single Mechanism for Generating Large-Scale Structure and Providing Dark Missing Matter, *Phys. Rev. Lett.* **64**, 1084 (1990).
- [74] S.-J. Sin, Late time cosmological phase transition and galactic halo as Bose liquid, *Phys. Rev. D* **50**, 3650 (1994).
- [75] W. Hu, R. Barkana, and A. Gruzinov, Cold and Fuzzy Dark Matter, *Phys. Rev. Lett.* **85**, 1158 (2000).

- [76] L. Hui, J. P. Ostriker, S. Tremaine, and E. Witten, Ultralight scalars as cosmological dark matter, *Phys. Rev. D* **95**, 043541 (2017).
- [77] J.-W. Lee, Brief history of ultra-light scalar dark matter models, *EPJ Web Conf.* **168**, 06005 (2018).
- [78] H.-Y. Schive, T. Chiueh, and T. Broadhurst, Cosmic structure as the quantum interference of a coherent dark wave, *Nat. Phys.* **10**, 496 (2014).
- [79] H.-Y. Schive, M.-H. Liao, T.-P. Woo, S.-K. Wong, T. Chiueh, T. Broadhurst, and W.-Y. P. Hwang, Understanding the Core-Halo Relation of Quantum Wave Dark Matter from 3D Simulations, *Phys. Rev. Lett.* **113**, 261302 (2014).
- [80] B. Schwabe, J. C. Niemeyer, and J. F. Engels, Simulations of solitonic core mergers in ultralight axion dark matter cosmologies, *Phys. Rev. D* **94**, 043513 (2016).
- [81] J. Veltmaat and J. C. Niemeyer, Cosmological particle-in-cell simulations with ultralight axion dark matter, *Phys. Rev. D* **94**, 123523 (2016).
- [82] P. Mocz, M. Vogelsberger, V. H. Robles, J. Zavala, M. Boylan-Kolchin, A. Fialkov, and L. Hernquist, Galaxy formation with BECDM—I. Turbulence and relaxation of idealized haloes, *Mon. Not. R. Astron. Soc.* **471**, 4559 (2017).
- [83] R. Ferrell and M. Gleiser, Gravitational atoms: Gravitational radiation from excited boson stars, *Phys. Rev. D* **40**, 2524 (1989).
- [84] S.-J. Sin, Late-time phase transition and the galactic halo as a bose liquid, *Phys. Rev. D* **50**, 3650 (1994).
- [85] S. U. Ji and S. J. Sin, Late-time phase transition and the galactic halo as a bose liquid. II. The effect of visible matter, *Phys. Rev. D* **50**, 3655 (1994).
- [86] D. F. Torres, S. Capozziello, and G. Lambiase, Super-massive boson star at the galactic center?, *Phys. Rev. D* **62**, 104012 (2000).
- [87] F. E. Schunck and D. F. Torres, Boson stars with generic selfinteractions, *Int. J. Mod. Phys. D* **09**, 601 (2000).
- [88] P. Amaro-Seoane, J. Barranco, A. Bernal, and L. Rezzolla, Constraining scalar fields with stellar kinematics and collisional dark matter, *J. Cosmol. Astropart. Phys.* **11** (2010) 002.
- [89] A. Bernal, J. Barranco, D. Alic, and C. Palenzuela, Multistate boson stars, *Phys. Rev. D* **81**, 044031 (2010).
- [90] D. H. Weinberg, J. S. Bullock, F. Governato, R. Kuzio de Naray, and A. H. G. Peter, Cold dark matter: Controversies on small scales, *Proc. Natl. Acad. Sci. U.S.A.* **112**, 12249 (2015).
- [91] D. J. E. Marsh and A.-R. Pop, Axion dark matter, solitons and the cusp–core problem, *Mon. Not. R. Astron. Soc.* **451**, 2479 (2015).
- [92] V. Iršič, M. Viel, M. G. Haehnelt, J. S. Bolton, and G. D. Becker, First Constraints on Fuzzy Dark Matter from Lyman- α Forest Data and Hydrodynamical Simulations, *Phys. Rev. Lett.* **119**, 031302 (2017).
- [93] L. A. Ureña López, V. H. Robles, and T. Matos, Mass discrepancy-acceleration relation: A universal maximum dark matter acceleration and implications for the ultralight scalar dark matter model, *Phys. Rev. D* **96**, 043005 (2017).
- [94] K.-H. Leong, H.-Y. Schive, U.-H. Zhang, and T. Chiueh, Testing extreme-axion wave-like dark matter using the BOSS Lyman-alpha forest data, *Mon. Not. R. Astron. Soc.* **484**, 4273 (2019).
- [95] N. Bar, D. Blas, K. Blum, and S. Sibiryakov, Galactic rotation curves versus ultralight dark matter: Implications of the soliton-host halo relation, *Phys. Rev. D* **98**, 083027 (2018).
- [96] N. Bar, K. Blum, J. Eby, and R. Sato, Ultralight dark matter in disk galaxies, *Phys. Rev. D* **99**, 103020 (2019).
- [97] M. Safarzadeh and D. N. Spergel, Ultra-light dark matter is incompatible with the milky way’s dwarf satellites, *Astrophys. J.* **893**, 21 (2020).
- [98] K. Schutz, Subhalo mass function and ultralight bosonic dark matter, *Phys. Rev. D* **101**, 123026 (2020).
- [99] M. Benito, J. C. Criado, G. Hütsi, M. Raidal, and H. Veermäe, Implications of Milky Way substructures for the nature of dark matter, *Phys. Rev. D* **101**, 103023 (2020).
- [100] H. N. Luu, S. H. H. Tye, and T. Broadhurst, Multiple ultralight axionic wave dark matter and astronomical structures, *Phys. Dark Universe* **30**, 100636 (2020).
- [101] M. H. Chan and C. Fai Yeung, Model-independent constraints on ultralight dark matter from the SPARC Data, *Astrophys. J.* **913**, 25 (2021).
- [102] N. Bar, K. Blum, and C. Sun, Galactic rotation curves vs. ultralight dark matter II, *Phys. Rev. D* **105**, 083015 (2022).
- [103] H. Y. J. Chan, E. G. M. Ferreira, S. May, K. Hayashi, and M. Chiba, The diversity of core–halo structure in the fuzzy dark matter model, *Mon. Not. R. Astron. Soc.* **511**, 943 (2022).
- [104] E. Calabrese and D. N. Spergel, Ultra-light dark matter in ultra-faint dwarf galaxies, *Mon. Not. R. Astron. Soc.* **460**, 4397 (2016).
- [105] A. X. González-Morales, D. J. E. Marsh, J. Peñarrubia, and L. A. Ureña-López, Unbiased constraints on ultralight axion mass from dwarf spheroidal galaxies, *Mon. Not. R. Astron. Soc.* **472**, 1346 (2017).
- [106] N. Kan and K. Shiraishi, A Newtonian analysis of multi-scalar boson stars with large self-couplings, *Phys. Rev. D* **96**, 103009 (2017).
- [107] J. Eby, M. Leembruggen, L. Street, P. Suranyi, and L. C. R. Wijewardhana, Galactic condensates composed of multiple axion species, *J. Cosmol. Astropart. Phys.* **10** (2020) 020.
- [108] H.-K. Guo, K. Sinha, C. Sun, J. Swaim, and D. Vagie, Two-scalar Bose-Einstein condensates: From stars to galaxies, *J. Cosmol. Astropart. Phys.* **10** (2021) 028.
- [109] T. Matos and L. A. Ureña-Lopez, Flat rotation curves in scalar field galaxy halos, *Gen. Relativ. Gravit.* **39**, 1279 (2007).
- [110] A. Bernal, J. Barranco, D. Alic, and C. Palenzuela, Multistate boson stars, *Phys. Rev. D* **81**, 044031 (2010).
- [111] L. A. Ureña-Lopez and A. Bernal, Bosonic gas as a galactic dark matter halo, *Phys. Rev. D* **82**, 123535 (2010).
- [112] S.-C. Lin, H.-Y. Schive, S.-K. Wong, and T. Chiueh, Self-consistent construction of virialized wave dark matter halos, *Phys. Rev. D* **97**, 103523 (2018).
- [113] F. S. Guzmán and L. A. Ureña López, Gravitational atoms: General framework for the construction of multistate axially symmetric solutions of the schrödinger-poisson system, *Phys. Rev. D* **101**, 081302 (2020).

- [114] L. Street, P. Suranyi, and L. C. R. Wijewardhana, Density profile of multi-state fuzzy dark matter, [arXiv:2101.00349](https://arxiv.org/abs/2101.00349).
- [115] F. S. Guzman and L. A. Urena-Lopez, Gravitational cooling of self-gravitating Bose-Condensates, *Astrophys. J.* **645**, 814 (2006).
- [116] A. Arbey, J. Lesgourgues, and P. Salati, Galactic halos of fluid dark matter, *Phys. Rev. D* **68**, 023511 (2003).
- [117] J.-w. Lee and I.-g. Koh, Galactic halos as boson stars, *Phys. Rev. D* **53**, 2236 (1996).
- [118] M. A. Amin, M. Jain, R. Karur, and P. Mocz, Small-scale structure in vector dark matter, [arXiv:2203.11935](https://arxiv.org/abs/2203.11935).
- [119] A. Khmelnitsky and V. Rubakov, Pulsar timing signal from ultralight scalar dark matter, *J. Cosmol. Astropart. Phys.* **02** (2014) 019.
- [120] I. De Martino, T. Broadhurst, S.H. Henry Tye, T. Chiueh, H.-Y. Schive, and R. Lazkoz, Recognizing Axionic Dark Matter by Compton and de Broglie Scale Modulation of Pulsar Timing, *Phys. Rev. Lett.* **119**, 221103 (2017).
- [121] PPTA Collaboration, Parkes pulsar timing array constraints on ultralight scalar-field dark matter, *Phys. Rev. D* **98**, 102002 (2018).
- [122] A. Aoki and J. Soda, Pulsar timing signal from ultralight axion in $f(R)$ theory, *Phys. Rev. D* **93**, 083503 (2016).
- [123] L. Street, N. Y. Gnedin, and L. C. R. Wijewardhana, DM halo models, https://github.com/laurenstreet/DM_halo_models.
- [124] J. Einasto, On the construction of a composite model for the galaxy and on the determination of the system of galactic parameters, *Tr. Astrofiz. Inst. Alma-Ata* **5**, 87 (1965).
- [125] J. F. Navarro, E. Hayashi, C. Power, A. R. Jenkins, C. S. Frenk, S. D. M. White, V. Springel, J. Stadel, and T. R. Quinn, The inner structure of Λ CDM haloes—III. Universality and asymptotic slopes, *Mon. Not. R. Astron. Soc.* **349**, 1039 (2004).
- [126] M. Newville, T. Stensitzki, D. B. Allen, and A. Ingargiola, LMFIT: Non-Linear Least-Square Minimization and Curve-Fitting for Python, [10.5281/zenodo.11813](https://zenodo.org/record/11813) (2014).
- [127] E. O. Lebigot, Uncertainties: A PYTHON package for calculations with uncertainties, <https://github.com/lebigot/uncertainties>.
- [128] G. Schwarz, Estimating the dimension of a model, *Ann. Stat.* **6**, 461 (1978).
- [129] A. R. Liddle, Information criteria for astrophysical model selection, *Mon. Not. R. Astron. Soc.* **377**, L74 (2007).
- [130] H. Jeffreys, *Theory of Probability*, 3rd ed. (Oxford University Press, Oxford, 1961).
- [131] N. Dalal and A. Kravtsov, Not so fuzzy: Excluding FDM with sizes and stellar kinematics of ultra-faint dwarf galaxies, [arXiv:2203.05750](https://arxiv.org/abs/2203.05750).